
PHOTOEMISSION
DISTRIBUTIONS FROM
TIME-DEPENDENT DENSITY
FUNCTIONAL THEORY

Masterarbeit

zur Erlangung des akademischen Grades eines

Master of Science

an der naturwissenschaftlichen Fakultät der
Karl-Franzens-Universität Graz

August 2022



vorgelegt von

Dominik BRANDSTETTER,
BSc.

Betreuer

Peter PUSCHNIG,
Assoz.-Prof. Dr.

Acknowledgement

I would like to express my sincere gratitude to my supervisor Peter Puschnig for his assistance at every stage of the research project. Furthermore, I am deeply grateful to Christian Kern, Andreas Windischbacher, Masoud Hamidi and Mathias Schwendt for their insightful comments and suggestions. Last but not least, I would like to offer my special thanks to my family, in particular Christof Brandstetter and Daniela Palk for their unwavering support and belief in me.

Abstract

A recent study in photoemission orbital tomography [Science 371, 1056 (2021)] has demonstrated that transiently excited electrons can be traced in time. This has become possible through measuring their signature in the angle-resolved momentum distribution of photoelectrons released by a high-energy probe pulse. Further developing this exciting and powerful new technique, dubbed orbital cinematography, is a desirable track for future experimental development. In this work, we use time-dependent density functional theory to scout ahead and perform an ab-initio simulation of a sub-femtosecond pump-probe angle-resolved photoemission experiment. We investigate potential issues and possible remedies in the description of ARPES within the framework of TD-DFT and conclude with momentum maps of the frontier orbitals.

Zusammenfassung

In einer kürzlich erschienenen Publikation zum Thema “Photoemission Orbital Tomography” [Science 371, 1056 (2021)] konnte gezeigt werden, dass es möglich ist kurzlebig angeregte Elektronen zeitlich aufzulösen. Dies geschieht durch Messung der winkelaufgelösten Impulsdistributionen der durch einen Laser freigesetzten Photoelektronen. Eine Weiterentwicklung dieser als “Orbital Cinematography” getauften Methode erscheint als eine erstrebenswerte Richtung für zukünftige experimentelle Forschung. Diese Arbeit greift solchen Bestrebungen durch Simulation eines sub-femtosekunden, “pump-probe”, winkelaufgelösten Photoemissionsexperiments mittels “Time-dependent Density Functional Theory” vor. Untersucht werden potentielle Probleme die sich aus der theoretischen Beschreibung von “ARPES” im Rahmen von “TD-DFT” ergeben, und wie diese möglicherweise gelöst werden können. Am Ende dieser Arbeit stehen Impulskarten im Grundzustand besetzter und unbesetzter Orbitale nahe der Fermikante.

Contents

1	Introduction	6
2	Theory	9
2.1	Density Functional Theory	9
2.1.1	Geometry Optimization	12
2.2	Time-Dependent Density Functional Theory	13
2.2.1	TD-DFT Basics	13
2.2.2	Linear Response	17
2.2.3	Description of Photoemission in TD-DFT	20
2.2.4	Ehrenfest Dynamics	22
2.3	Rabi Oscillation	23
2.3.1	Mollow-(like) Triplets	27
2.3.2	Failure of TD-DFT	28
3	Results	31
3.1	Computational Setup	31
3.1.1	Octopus	31
3.1.2	GPAW	32
3.1.3	VSC-3	32
3.2	Geometry Optimization	34
3.3	Optical Response	35
3.4	LUMO Occupation	40
3.5	Photoemission Data	51
3.6	Ehrenfest Dynamics	64
4	Conclusion and Future Prospects	66
A	Example usage: Octopus	68
B	Example usage: GPAW	73
C	Low Kinetic Energy Emissions	75
D	Octopost	79
	List of Figures	80
	References	81

1 Introduction

With the advent of photoemission orbital tomography (POT)[1, 2, 3], pioneered by Puschnig, Ramsey and Tautz, theoretical electronic structure calculations have been shown to provide aid in the interpretation of angle-resolved photoemission spectra (ARPES) in the form of momentum maps. Relying on the plane-wave final state approximation, POT celebrated a number successful applications, e.g., in the clarification of the aromaticity of kekulene [4], imaging σ -orbitals in organic molecules [5] and demonstrating the importance of charge transfer for the self-metalation of porphyrin [6], just to list a few. Moreover, in a recent publication Wallauer et al. [7] were able to showcase the possibility of tracing the momentum maps of frontier orbitals, when pushed out of the groundstate with a pump laser, on a femtosecond timescale. Following these lines, the next innovation could be on the horizon: “orbital cinematography”. It promises to yield slow-motion videos of the movement of electrons in the frontier orbitals of organic molecules.

A particularly challenging endeavour will be the investigation of sub-femtosecond electron dynamics in organic molecules, thereby answering fundamental questions on optical induced charge transfer and spatiotemporal superpositions of molecular orbitals. On the example of a quarterphenyl molecule, adding electron-pushing and -pulling substituents at the ends of the molecule introduces a fundamental asymmetry in the frontier orbitals along the long axis of the molecule. Specifically, the highest occupied molecular orbital (HOMO) and lowest unoccupied molecular orbital (LUMO) show an increased localization on either side of the molecule and a transition between them, induced by a pump pulse at a suitable energy, will drive an intramolecular charge transfer. This charge transfer will then be probed at various stages in time with a second high-energy sub-femtosecond laser that releases an electron from the molecule. The angular distribution of these emitted electrons, the so-called momentum maps, allows the entire charge transfer process to be tracked in time.

This, however, pushes the static theoretical description of the photoemission process with POT to its limits. The time dependence introduced in the experiment with a pump-probe laser setup is missing completely in POT, as well as, in general, the interaction of the freed electrons with the remaining electrons and with the electromagnetic field. At this point, time-dependent density functional theory (TD-DFT) has been demonstrated to provide a more advanced simulation of the entire process, from the excitation of the groundstate to the propagation of the freed electrons to detector, in time [8].

This thesis is an early attempt on predicting possible results, issues and unaccounted physical (and numerical) phenomena that might be observed in such sub-femtosecond charge-transfer dynamics by ab-initio simulations of ARPES in time-dependent density functional theory.

Molecule

The molecule investigated here is 4-Amino-4'-nitrobiphenyl (see Figure 1), a chemically close relative of the quarterphenyl derivative described above. In the following we will refer to this molecule as “ANBP” as abbreviation. It

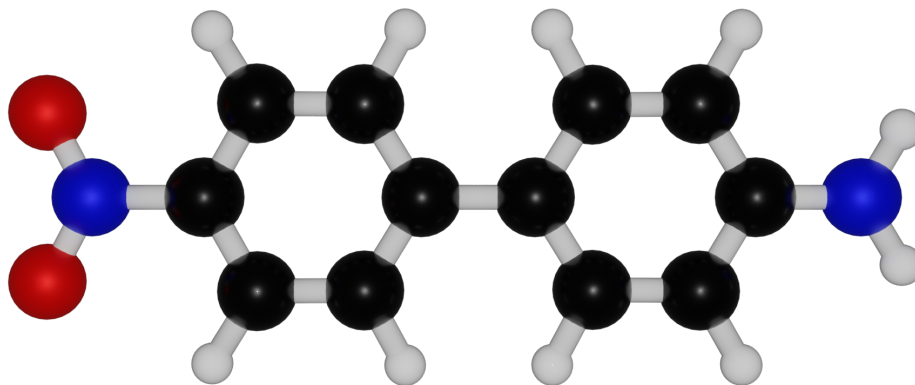
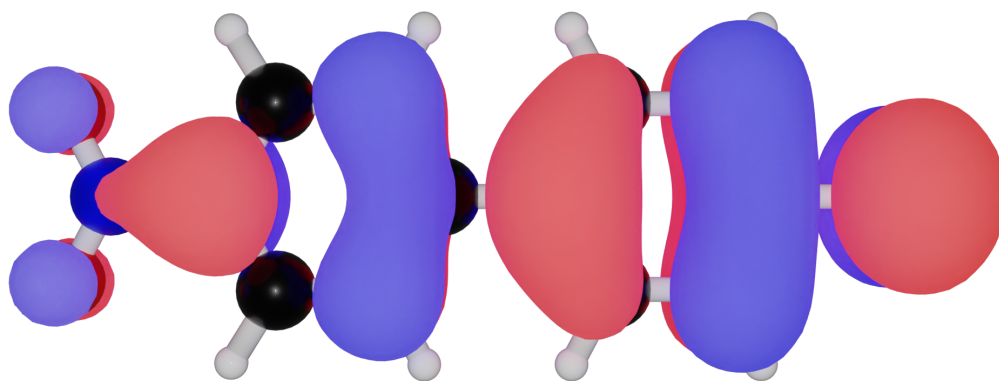


Figure 1: 4-Amino-4'-nitrobiphenyl, a chemically close relative of the molecule above-mentioned, but with a shorter backbone to facilitate computations. The electron pushing group (amine) is connected to the rightmost carbon labelled 4 by standard chemical nomenclature, the electron pulling group (nitro) is attached to the leftmost carbon 4'. The central inter-ring bond is the $C_1 - C_{1'}$ bond.

too shows the important asymmetry along the long axis between HOMO and LUMO, as can be seen from a density functional calculation of the ground-state Kohn-Sham orbitals in Figure 2. Its much reduced spatial extent in one direction and lower overall number of states significantly reduces the computational cost of all calculations, without sacrificing any core feature of the original quarterphenyl derivative relevant for future experiments.

(a) HOMO



(b) LUMO

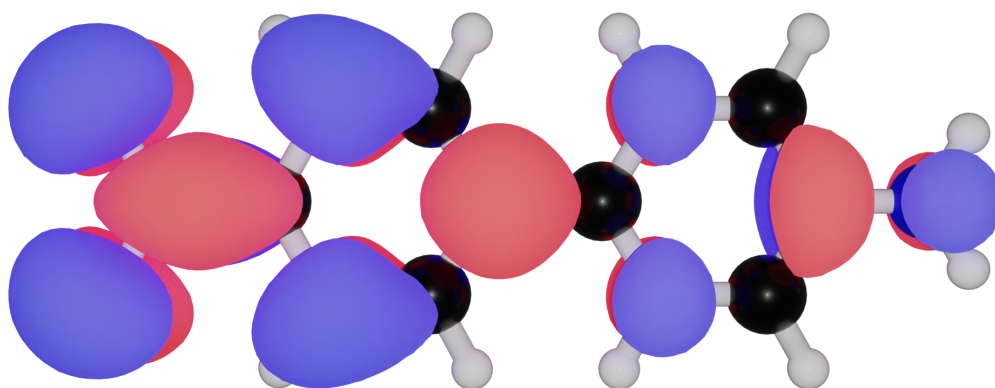


Figure 2: The highest occupied molecular orbital (HOMO, top) and lowest unoccupied molecular orbital (LUMO, bottom) as result of groundstate density functional theory. The HOMO shows a localization of electrons on the amine group (right), while the LUMO reverses this localization in favour of the nitro group.

2 Theory

2.1 Density Functional Theory

In this chapter, a brief summary of density functional theory (DFT) will be given to provide the reader with the basic vocabulary used throughout this thesis. For a more thorough introduction please refer to Refs. [9, 10, 11].

Hohenberg-Kohn Theorems

One core task in solid state physics and modern quantum chemistry is to describe the valence electrons in individual molecules, clusters of molecules or solid phases of matter. This quantum mechanical many-body problem is defined by the time-independent Schrödinger equation

$$\left[\underbrace{-\frac{1}{2} \sum_{i=1}^N \nabla_i^2}_{\hat{T}} + \underbrace{\sum_{i=1}^N \sum_{j<i} \frac{1}{|\mathbf{r}_i - \mathbf{r}_j|}}_{\hat{V}^{ee}} + \sum_{i=1}^N \hat{v}^{\text{ext.}}(\mathbf{x}_i) \right] \Psi(\{\mathbf{x}_i\}) = E \Psi(\{\mathbf{x}_i\}) \quad (1)$$

for a system of N interacting electrons feeling the influence of the positively charged nuclei. Here \hat{T} , \hat{V}^{ee} and $\hat{v}^{\text{ext.}}(\mathbf{x})$ are the operators for the kinetic energy of the electrons, the Coulomb repulsion between individual electrons and the electron-nucleus interaction, respectively, and $\mathbf{x}_i = (\mathbf{r}_i, \sigma_i)$ denotes the spatial and spin coordinate of the i -th electron. By asserting the existence of an electronic wavefunction $\Psi(\{\mathbf{x}_i\})$ with no functional dependence on the nuclear coordinates, we implicitly applied the Born-Oppenheimer approximation. The electrons are assumed to move in the instantaneous field of the nuclei frozen in time.

Not only is it not possible to solve this equation analytically for more than one electron (i.e. Hydrogen atom), even the memory requirements for storing the full many-body wavefunction $|\Psi(\{\mathbf{x}_i\})\rangle$ of a small molecule on a modest numerical grid gets out of hand exponentially [9].

Density functional theory is one approach to simplify this problem by moving away from the many-body wavefunction entirely and instead focusing on the electron density, which is related to the many-electron wave function of in the following way:

$$n(\mathbf{x}) = N \sum_{\{\sigma_i\}} \int d^3r \int d^3r_2 \cdots \int d^3r_N |\Psi(\mathbf{x}, \mathbf{x}_2, \cdots, \mathbf{x}_N)|^2.$$

It can be easily interpreted as the as the number of electron $dN = n(\mathbf{x}) d\mathbf{x}$ in the coordinate interval $d\mathbf{x}$. The usefulness of the electron density as a basic

variable is guaranteed by the first theorem of Hohenberg and Kohn [12]. It states that the groundstate density uniquely determines all groundstate properties of the system [9]. The individual terms in Equation (1) are now functionals of the electron density.

Kohn-Sham Equations

Even though replacing the many-body wavefunction with the electron density has simplified the problem of solving Equation (1), a completely orbital-free approach is still not trivial to do. One main reason is the difficulty in constructing a quantum mechanical kinetic energy functional $\hat{T}[n](\mathbf{r})$ solely in terms of the electron density [13].

To circumvent the aforementioned difficulty, Kohn and Sham [14] proposed the following: Consider the hypothetical case of N non-interacting electrons in an effective single-particle “Kohn-Sham potential” $\hat{v}^{\text{KS}}[n](\mathbf{x})$ which we call “Kohn-Sham system”. The Hamiltonian \hat{H}^{KS} , therefore, decomposes into single particle Hamiltonians

$$\begin{aligned}\hat{h}^{\text{KS}}\varphi_i^{\text{KS}}(\mathbf{x}) &= \left[-\frac{1}{2}\nabla^2 + \hat{v}^{\text{KS}}[n](\mathbf{x}) \right] \varphi_i^{\text{KS}}(\mathbf{x}) \\ &= \epsilon_i \varphi_i^{\text{KS}}(\mathbf{x}),\end{aligned}\tag{2}$$

with single-electron eigenstates $\varphi_i^{\text{KS}}(\mathbf{x})$ (“Kohn-Sham orbitals”) and eigenenergies ϵ_i . This reintroduces orbitals into DFT, however, one has to be careful with the interpretation of them as physical quantities. In practice, (occupied) Kohn-Sham orbitals often resemble molecular orbitals from Hartree-Fock or Hückel models [15]. It should be noted that, Kohn-Sham energies can be interpreted using Janak’s theorem [16].

The wavefunction for the entire system $\Psi^{\text{KS}}(\{\mathbf{x}_i\})$ is then a single Slater determinant [10]

$$\Psi^{\text{KS}}(\{\mathbf{x}_i\}) = \frac{1}{\sqrt{N!}} \begin{vmatrix} \varphi_1^{\text{KS}}(\mathbf{x}_1) & \cdots & \varphi_1^{\text{KS}}(\mathbf{x}_N) \\ \vdots & & \vdots \\ \varphi_N^{\text{KS}}(\mathbf{x}_1) & \cdots & \varphi_N^{\text{KS}}(\mathbf{x}_N) \end{vmatrix}.\tag{3}$$

To calculate the properties of the real system from the Kohn-Sham system, $\hat{v}^{\text{KS}}[n](\mathbf{x})$ is constructed in such a way, that the resulting electron density $n^{\text{KS}}(\mathbf{x})$ is identical to density of the real system $n(\mathbf{x})$

$$\hat{v}^{\text{KS}}[n](\mathbf{x}) := \hat{v}^{\text{H}}[n](\mathbf{r}) + \hat{v}^{\text{ext.}}[n](\mathbf{x}) + \hat{v}^{\text{xc}}[n](\mathbf{x})\tag{4}$$

$$\Rightarrow n^{\text{KS}}(\mathbf{x}) = \sum_{i=1}^N |\varphi_i^{\text{KS}}(\mathbf{x})|^2 \stackrel{!}{=} n(\mathbf{x})\tag{5}$$

This includes known terms like the Hartree potential

$$\hat{v}^H [n] (\mathbf{r}) = \int \frac{n(\mathbf{r}')}{|\mathbf{r} - \mathbf{r}'|} d^3r',$$

accounting for the classical electron-electron interaction and the external potential $\hat{v}^{\text{ext.}} [n] (\mathbf{x})$. Equation (4) can also be seen as the definition of the notorious “exchange-correlation functional” $\hat{v}^{\text{xc}} [n] (\mathbf{x})$.

With the above scheme, we have reduced the many-body fully interacting problem Equation (1) to solve a system of coupled single-electron Schrödinger Equations (2). Because the Kohn-Sham potential, Equation (4), necessary to solve the Kohn-Sham equations (KSE) depends, via the density (5), on the solutions to the KSE, this has to be solved self-consistently (“SCF-cycle”) with an initial guess and a convergence criteria depended on the property in question (e.g. total energy, density, ...).

Exchange-correlation potential

The procedure to solve the KSE outlined in the previous paragraph relies on the knowledge of the correct form of the xc-functional $\hat{v}^{\text{xc}} [n] (\mathbf{x})$ introduced in Equation (4). It is supposed to account for the “exchange energy” already present in Hartree-Fock theory and all other effects yet to be added to recover the fully interacting system, collectively dubbed “correlation energy”. Up to this point, DFT is an exact reformulation of the time-independent quantum mechanics of the electronic structure problem. For the xc-functional, whose existence is guaranteed by the theorems of Kohn and Sham [9], however, only approximations of different sophistication and intended use are available. Note that, the xc-potential is spin-dependent and, in general, non-local in nature.

Here we only mention the most simple, yet ubiquitous, approximation already proposed by Kohn and Sham [17] called “local density approximation (LDA)”

$$\hat{v}^{\text{LDA}} [n] (\mathbf{r}) = \int d^3r' n(\mathbf{r}') \hat{v}^{\text{unif.}} (n(\mathbf{x}')). \quad (6)$$

Here $\hat{v}^{\text{unif.}} (n(\mathbf{x}))$ is the exchange-correlation energy per electron in a homogeneous uniform electron gas (jellium model) with a constant density $n(\mathbf{x}) = n$. Results obtained with an LDA approximation are often in surprisingly good agreement with more sophisticated functionals, even for non-metallic systems with electronic structures more distant to the uniform electron model it is based on.

2.1.1 Geometry Optimization

Density functional theory, like many other electronic structure models, builds upon the Born-Oppenheimer approach, separating the movement of the nuclei from the movement of the electrons by “freezing” the position of the former. However, if the geometry of the system is not already in equilibrium, forces on the individual atoms will occur trying to relax the structure. From the full Hamiltonian of the system

$$\hat{H} = -\frac{1}{2} \sum_{i=1}^N \nabla_i^2 + \sum_{i=1}^N \sum_{j<i} \frac{1}{|\mathbf{r}_i - \mathbf{r}_j|} - \sum_{i=1}^N \sum_{J=1}^K \frac{Z_J}{|\mathbf{r}_i - \mathbf{R}_J|} + \sum_{I=1}^N \sum_{J<I}^K \frac{Z_I Z_J}{|\mathbf{R}_I - \mathbf{R}_J|},$$

we can calculate the force \mathbf{F}_J on the nuclei J as

$$\begin{aligned} \mathbf{F}_J &= -\frac{dE(\{\mathbf{R}_I\})}{d\mathbf{R}_J} \\ &= -\frac{d}{d\mathbf{R}_J} \langle \Psi | \hat{H}(\{\mathbf{R}_I\}) | \Psi \rangle \\ &= -\langle \Psi | \frac{d\hat{H}(\{\mathbf{R}_I\})}{d\mathbf{R}_J} | \Psi \rangle \\ &= \int d^3r n(\mathbf{r}) \frac{Z_J(\mathbf{r} - \mathbf{R}_J)}{|\mathbf{r} - \mathbf{R}_J|^3} + \sum_{J \neq K} \frac{Z_K Z_J (\mathbf{R}_K - \mathbf{R}_J)}{|\mathbf{R}_K - \mathbf{R}_J|^3}, \end{aligned}$$

where in the second to last step we used the Hellmann-Feynman theorem [10]. Thus, with the groundstate electron density $n(\mathbf{r})$ from a converged DFT calculation, one can calculate all the forces and iteratively relax the ionic positions, until an energy minimum with respect to the nuclear coordinates is reached. This approach is also sometimes called “damped Born-Oppenheimer molecular dynamics” [18]. Damped refers to an added artificial damping factor that prevents the ions from oscillating around the equilibrium position.

2.2 Time-Dependent Density Functional Theory

In the following chapter, we show how density functional theory can be extended to the time-dependent case (Chapter 2.2.1). With time-dependent external potentials one can model light-matter interaction (Chapter 2.2.2) and the subsequent photoemission process (Chapter 2.2.3) directly, without assuming a final state.

2.2.1 TD-DFT Basics

For details on the matter discussed below, refer to the References [11, 19, 20] used throughout the following chapter. Starting from the many-electron Hamiltonian \hat{H}_0 defined in Equation (1), we can add a time-dependent potential $\hat{v}^{\text{TD}}(\mathbf{x}, t)$ to the previously static Hamiltonian \hat{H}_0

$$\hat{H} = \underbrace{\hat{T} + \hat{V}^{ee}}_{\hat{H}_0} + \underbrace{\sum_{i=1}^N \hat{v}^{\text{ext.}}(\mathbf{x}_i)}_{\sum_i \hat{v}^{\text{ext.}}(\mathbf{x}_i, t)} + \underbrace{\sum_{i=1}^N \hat{v}^{\text{TD}}(\mathbf{x}_i, t)}_{\hat{H}'}.$$

Using this time-dependent Hamiltonian, we seek a solution of the time-dependent Schrödinger equation

$$\hat{H} |\Psi(\{\mathbf{x}_i\}, t)\rangle = i\partial_t |\Psi(\{\mathbf{x}_i\}, t)\rangle.$$

For the same reasons as in the static case, we would like to trade the many-body wavefunction $\Psi(\{\mathbf{x}_i\}, t)$ for the electron-density $n(\mathbf{x}, t)$ first and subsequently introduce single-particle Kohn-Sham orbitals $\varphi_i^{\text{KS}}(\mathbf{x}, t)$, analogous to groundstate DFT. The Hohenberg-Kohn theorems used to prove that the density is in fact a valid replacement relies on the Rayleigh-Ritz variational principle, in that the correct groundstate density will minimize the energy functional. This no longer holds for the time-dependent case.

Runge-Gross Theorem

There is, however, an analogous theorem in TD-DFT, namely the Runge-Gross theorem, which replaces the theorems by Hohenberg-Kohn. It states that for a given initial state $\Psi_0 = \Psi(\{\mathbf{x}_i\}, 0)$ there is a one-to-one mapping between the external potential $\hat{v}^{\text{ext.}}(\mathbf{x}_i, t)$ and the density $n(\mathbf{x}, t)$, up to a time-dependent additive term. This term will result only in a time-dependent phase factor for the wavefunction, which has no consequence for

the density [19]. Solutions to the Schrödinger equation are unique and, therefore, this relation is trivial in the direction $\hat{v}^{\text{ext.}} \rightarrow n$, with the definition of the density

$$n(\mathbf{x}, t) = N \sum_{\{\sigma_i\}} \int d^3r \int d^3r_2 \cdots \int d^3r_N |\Psi(\mathbf{x}, \mathbf{x}_2, \dots, \mathbf{x}_N, t)|^2.$$

The proof for the inverse direction is outlined as follows:

Consider the Heisenberg equation of motion for the expectation value $\mathbf{j}(\mathbf{x}, t)$ of the current-density operator $\hat{\mathbf{j}}(\mathbf{x})$

$$\begin{aligned} \mathbf{j}(\mathbf{x}, t) &= \langle \Psi(\{\mathbf{x}_i\}, t) | \hat{\mathbf{j}}(\mathbf{x}) | \Psi(\{\mathbf{x}_i\}, t) \rangle \\ \hat{\mathbf{j}}(\mathbf{x}) &= -\frac{i}{2} \sum_{i=1}^N [\nabla_i \delta(\mathbf{r} - \mathbf{r}_i) + \delta(\mathbf{r} - \mathbf{r}_i) \nabla_i] \end{aligned} \quad (7)$$

$$\Rightarrow \frac{\partial}{\partial t} \mathbf{j}(\mathbf{x}, t) = i \langle \Psi(\{\mathbf{x}_i\}, t) | [\hat{H}, \hat{\mathbf{j}}(\mathbf{x})] | \Psi(\{\mathbf{x}_i\}, t) \rangle. \quad (8)$$

We assume two external potentials $\hat{v}^{\text{ext.}}(\mathbf{x}, t)$, that differ by more than a time-dependent term

$$\hat{w}(\mathbf{x}, t) := \hat{v}^{\text{ext.}}(\mathbf{x}, t) - \tilde{v}^{\text{ext.}}(\mathbf{x}, t) \neq \hat{w}(t), \quad (9)$$

from a common (not necessarily groundstate) initial state $|\Psi_0\rangle = |\Psi(\{\mathbf{x}_i\}, 0)\rangle$. Because these two Kohn-Sham systems differ only in the external potential, the following yields

$$\begin{aligned} \left. \frac{\partial}{\partial t} [\mathbf{j}(\mathbf{x}, t) - \tilde{\mathbf{j}}(\mathbf{x}, t)] \right|_{t=0} &= i \langle \Psi_0 | [\hat{v}^{\text{ext.}}(\mathbf{x}, 0) - \tilde{v}^{\text{ext.}}(\mathbf{x}, 0), \hat{\mathbf{j}}(\mathbf{x})] | \Psi_0 \rangle \\ &= n(\mathbf{x}, 0) \nabla w(\mathbf{x}, 0). \end{aligned} \quad (10)$$

This means that if condition (9) is fulfilled, the two current densities will evolve differently at $t > 0$.¹ Using the continuity equation

$$\frac{\partial}{\partial t} n(\mathbf{x}, t) = -\nabla \cdot \mathbf{j}(\mathbf{x}, t), \quad (11)$$

we can reformulate the result of Equation (10) in terms of the electron density by computing the gradient of Equation (10)

$$\left. \frac{\partial^2}{\partial t^2} [n(\mathbf{x}, t) - \tilde{n}(\mathbf{x}, t)] \right|_{t=0} = -\nabla \cdot [n(\mathbf{x}, 0) \nabla w(\mathbf{x}, 0)]. \quad (12)$$

¹By requiring Taylor-expandability and reformulating Equation (9), the original proof from Reference [19] also covers the case where the first derivative of $w(\mathbf{x}, t)$ vanishes by repeatedly applying Equation (8).

In order to show that the right hand side of Equation (12) cannot vanish under the assumption of Equation (9), we consider the following integral

$$\int d^3r w(\mathbf{x}, t) \nabla \cdot [n(\mathbf{x}, 0) \nabla w(\mathbf{x}, t)] = \int d^3r \nabla \cdot [w(\mathbf{x}, t) n(\mathbf{x}, 0) \nabla w(\mathbf{x}, t)] - \int d^3r n(\mathbf{x}, 0) [\nabla w(\mathbf{x}, t)]^2.$$

First, we notice that the first term on the right hand side can be rewritten into a surface integral using Gauss's theorem and thus vanishes for any reasonable density tending towards zero sufficiently fast. The integrand of the second term on the right hand side is strictly positive and, thus, the right hand side in Equation (12) cannot vanish either. This proves that the density for two different external potentials will evolve differently and, therefore, also the direction $n \rightarrow \hat{v}^{\text{ext}}$ for the one-to-one mapping holds, as the Runge-Gross theorem promised. Strictly speaking, this only proves the uniqueness of the external potential for a given density, not its existence. The same is true for the static case and is called “ v -representability problem” [11]. In practice this turns out not to be an issue.

Time-dependent Kohn-Sham Equations

In complete analogy to the static case, we again introduce a Kohn-Sham system of N non-interacting electrons under the influence of a KS-potential $\hat{v}^{\text{KS}}[n, \Phi_0](\mathbf{x}, t)$ that will lead to an identical electron density $n^{\text{KS}}(\mathbf{x}, t)$ as the fully interacting one

$$n^{\text{KS}}(\mathbf{x}, t) = \sum_{i=1}^N |\varphi_i^{\text{KS}}(\mathbf{x}, t)|^2 \stackrel{!}{=} n(\mathbf{x}, t).$$

The Kohn-Sham orbitals $\varphi_k^{\text{KS}}(\mathbf{x}, t)$ can then be shown to fulfil the time-dependent Schrödinger equations

$$i \frac{\partial}{\partial t} \varphi_k^{\text{KS}}(\mathbf{x}, t) = \left[-\frac{1}{2} \nabla^2 + \hat{v}^{\text{KS}}[n, \Phi_0](\mathbf{x}, t) \right] \varphi_k^{\text{KS}}(\mathbf{x}, t), \quad (13)$$

where the KS-potential is now also a functional of the initial state Φ_0 , which is usually constructed out of single-particle wavefunctions via a single Slater determinate (see Equation (3)). As we have done in groundstate DFT, the KS-potential is split into three parts

$$\hat{v}^{\text{KS}}[n, \Psi_0, \Phi_0](\mathbf{x}, t) = \hat{v}^{\text{H}}[n, \Psi_0](\mathbf{r}, t) + \hat{v}^{\text{ext.}}[n, \Psi_0](\mathbf{x}, t) + \hat{v}^{\text{xc}}[n, \Psi_0, \Phi_0](\mathbf{x}, t). \quad (14)$$

The Hartree potential $\hat{v}^{\text{H}} [n, \Psi_0] (\mathbf{r}, t)$ describes the classical interaction of a charge distribution with itself, which is now also time-dependent

$$\hat{v}^{\text{H}} [n, \Psi_0] (\mathbf{r}, t) = \int d^3 r' \frac{n(\mathbf{r}', t)}{|\mathbf{r} - \mathbf{r}'|}.$$

Note, that the Hartree potential does not take any retardation effects into account, as it depends on the instantaneous electron density only.

The external potential $\hat{v}^{\text{ext.}} [n, \Psi_0] (\mathbf{x}, t)$ is usually given by the Coulomb field from the nuclei and, therefore, has no explicit dependency on the initial state wavefunction Ψ_0 . The exchange-correlation potential will be discussed in more detail in the next paragraph.

In real-time TD-DFT, one uses the results of a converged DFT groundstate calculation as initial state Φ_0 and propagates the individual KS-orbitals according to Equation (13) in time via a numerical scheme for the time derivative, thus removing the necessity for a self-consistency cycle.

Exchange-Correlation Potential

The exchange-correlation potential $\hat{v}^{\text{xc}} [n, \Psi_0, \Phi_0] (\mathbf{x}, t)$ can only be approximated as there is no known explicit form. In fact, contrary to the other two potentials, it depends on the entire history of the electron density. This “memory” makes it not only particularly hard to write down, but also any computation would require an approximation anyhow.

It is this memory dependence that is neglected in almost all xc-functionals available, which is referred to as the “adiabatic approximation”. The argument goes like this: At any point in time t , the instantaneous electron density $n(\mathbf{x}, t)$ is the groundstate density of some other, unknown system. Thus, it is justified to apply the static xc-functional

$$\hat{v}_{\text{adia.}}^{\text{xc}} [n] (\mathbf{x}, t) = \hat{v}_{\text{GS}}^{\text{xc}} [n(t)] (\mathbf{x}).$$

This, however, is still a severe approximation and only really justified for systems starting in the groundstate and varying only slowly in time. Even if the density at the point $t > t_0$ could be reproduced by some system in its groundstate, the wavefunctions could not. Nevertheless, due to its simplicity, the reuse of an already existing, large catalogue of static xc-functionals and, last but not least, its success in most practical cases, the adiabatic approximation is ubiquitous in TD-DFT.

As a particularly simple and widely used approximation, we mention the adiabatic local density approximation ALDA. In comparison with the LDA for groundstate DFT defined in Equation (6), it is obtained by simply allowing for a time-dependent density, but keeping the structure of the functional

unchanged

$$\hat{v}^{\text{xc;ALDA}}[n](\mathbf{r}) = \hat{v}_{\text{GS}}^{\text{LDA}}[n(t)](\mathbf{r}) = \int d^3r' n(\mathbf{r}', t) \hat{v}^{\text{unif.}}[n(t)](\mathbf{r}).$$

2.2.2 Linear Response

Depending on the size of the basis set, the result of a ground state DFT calculation can include higher lying, unoccupied eigenstates with the eigenenergies ϵ_i of the static Kohn-Sham Hamiltonian \hat{h}^{KS} (Equation (2)). However, they cannot be identified with excited states of the fully interacting system [16]. Within the framework of linear-response theory, the simulation of the dynamics of the many-body effects during an excitation allows TD-DFT to better estimate the absorption spectrum of a system [21]. Here, we want to give a short overview of linear-response time-dependent density functional theory (LRTD-DFT) [21] and state Casida’s equation [21, 22], a formulation which is implemented in many modern quantum chemistry packages.

We consider an external time-dependent potential of the following form

$$\hat{v}^{\text{ext.}}[n](\mathbf{r}, t) = \hat{v}_0^{\text{ext.}}[n_0](\mathbf{r}) + \hat{v}_1^{\text{ext.}}[n](\mathbf{r}, t) \theta(t - t_0).$$

Thus, for $t < t_0$, the system experiences only a time-independent potential $\hat{v}_0^{\text{ext.}}[n_0](\mathbf{r})$ which we identify with, in general, the electrostatic influence of the frozen nuclei. An additional time-dependent external potential $\hat{v}_1^{\text{ext.}}[n](\mathbf{r}, t)$, switched on at $t = t_0$, induces an excitation in the system. The Runge-Gross theorem, then, guarantees a one-to-one mapping between the external potential $\hat{v}^{\text{ext.}}[n](\mathbf{r}, t)$, and, therefore, also the Kohn-Sham potential $\hat{v}^{\text{KS}}[n](\mathbf{x}, t)$, and the electron density $n(\mathbf{x}, t)$. We can, thus, formally invert Equation (14)

$$n(\mathbf{x}, t) = n[\hat{v}^{\text{KS}}](\mathbf{x}, t).$$

For a sufficiently weak perturbing field, we can expand the electron density $n(\mathbf{x}, t)$ in powers of $\hat{v}_1^{\text{ext.}}[n](\mathbf{r}, t)$

$$n(\mathbf{x}, t) = n_0(\mathbf{x}) + n_1(\mathbf{x}, t) + n_2(\mathbf{x}, t) + \dots$$

The first-order density response $n_1(\mathbf{x}, t)$ can then be expressed as

$$n_1(\mathbf{x}, t) = \int dt' \int d^4x' \chi^{\text{KS}}(\mathbf{x}, t, \mathbf{x}', t') \hat{v}_1^{\text{KS}}(\mathbf{x}', t'), \quad (15)$$

where we have introduced the “linear density-density response function”

$$\chi^{\text{KS}}[n_0](\mathbf{x}, t, \mathbf{x}', t') = \left. \frac{\delta n(\mathbf{x}, t)}{\delta \hat{v}^{\text{KS}}(\mathbf{x}', t')} \right|_{\hat{v}^{\text{KS}}[n_0]},$$

a functional of the groundstate density n_0 . The integral $\int d^4x$ has to be understood as the integration over all real space \mathbf{r} and a summation over the spin coordinate σ : $\sum_{\sigma} \int d^3r$. According to Equation (14), the first order Kohn-Sham potential can be expressed as

$$\hat{v}_1^{\text{KS}}[n](\mathbf{x}, t) = \hat{v}_1^{\text{ext.}}[n](\mathbf{r}, t) + \int d^3r' \frac{n_1(\mathbf{r}, t)}{|\mathbf{r} - \mathbf{r}'|} + \hat{v}_1^{\text{xc}}[n](\mathbf{x}, t).$$

For the last term, the first-order xc-potential,

$$\hat{v}_1^{\text{xc}}[n](\mathbf{x}, t) = \int dt' \int d^4x' \underbrace{\frac{\delta \hat{v}^{\text{xc}}[n](\mathbf{x}, t)}{\delta n(\mathbf{x}', t')}}_{f^{\text{xc}}[n_0](\mathbf{x}, t, \mathbf{x}', t')} \Big|_{n_0} n_1(\mathbf{x}', t'), \quad (16)$$

we introduce the important “time-dependent xc kernel” $f^{\text{xc}}[n_0](\mathbf{x}, t, \mathbf{x}', t')$, again a functional of the groundstate density n_0 . Note that the kernel, as well as the response function $\chi^{\text{KS}}(\mathbf{x}, t, \mathbf{x}', t')$, only depend on the time difference $t - t'$. Because we want to extract the excitation energies from the system, we will now switch to frequency space by Fourier transform to replace space, and replace the time difference $t - t'$ by the frequency ω as a basic variable. Introducing the “Hartree-xc kernel”

$$f^{\text{Hxc}}[n_0](\mathbf{x}, \mathbf{x}', \omega) = \frac{1}{|\mathbf{r} - \mathbf{r}'|} + \int d(t - t') e^{i\omega(t-t')} f^{\text{xc}}[n_0](\mathbf{x}, t, \mathbf{x}', t'),$$

and plugging Equation (16) into Equation (15)

$$n_1(\mathbf{x}, \omega) = \int d^4x' \chi^{\text{KS}}(\mathbf{x}, \mathbf{x}', \omega) \left[\hat{v}_1^{\text{ext.}}[n](\mathbf{r}', \omega) + \int d^4x'' f^{\text{Hxc}}[n_0](\mathbf{x}', \mathbf{x}'', \omega) n_1(\mathbf{x}'', \omega) \right]$$

yields an equation that has be solved self-consistently in $n_1(\mathbf{x}, \omega)$. The Kohn-Sham response function in frequency space can be expressed as

$$\chi^{\text{KS}}(\mathbf{x}, \mathbf{x}', \omega) = \delta_{\sigma, \sigma'} \sum_{j, k} (f_{k\sigma} - f_{j\sigma}) \frac{\varphi_{0, j}^{\text{KS}}(\mathbf{x}) \varphi_{0, k}^{\text{KS}*}(\mathbf{x}) \varphi_{0, j}^{\text{KS}*}(\mathbf{x}') \varphi_{0, k}^{\text{KS}}(\mathbf{x}')}{\omega - \omega_{jk\sigma} + i\eta}, \quad (17)$$

where $\omega_{jk\sigma} = \epsilon_{j\sigma} - \epsilon_{k\sigma}$ are the excitation energies of the Kohn-Sham groundstate, not to be confused with the excitation energies Ω_n of the true system given by the poles $\omega = \Omega_n$ in the density response $n_1(\mathbf{x}, \omega)$.

Casida's Equation

First derived in 1995 [22], Casida's equation is a very powerful formulation of of LR TD-DFT for finite systems. In the sense of eigenmodes, the system can show a finite response even with no external potential required. This can be understood by a Dirac δ -shaped kick at $t = -\infty$ and the system, subsequently, sustaining a finite oscillation. For real groundstate orbitals Casida's equation is an eigenvalue equation

$$\begin{pmatrix} \mathbb{A} & \mathbb{B} \\ \mathbb{B} & \mathbb{A} \end{pmatrix} \begin{pmatrix} X \\ Y \end{pmatrix} = \Omega \begin{pmatrix} -\mathbb{1} & 0 \\ 0 & \mathbb{1} \end{pmatrix} \begin{pmatrix} X \\ Y \end{pmatrix}, \quad (18)$$

where the matrices \mathbb{A} and \mathbb{B} are defined by in the following way

$$\mathcal{A}_{ia\sigma, i'a'\sigma'}(\Omega) = \delta_{ii'} \delta_{aa'} \delta_{\sigma\sigma'} \omega_{a'i'\sigma'} + K_{ia\sigma, i'a'\sigma'}(\Omega)$$

$$\mathcal{B}_{ia\sigma, i'a'\sigma'}(\Omega) = K_{ia\sigma, i'a'\sigma'}(\Omega)$$

$$K_{ia\sigma, i'a'\sigma'}(\Omega) = \int d^4x \int d^4x' \varphi_{0,i}^{\text{KS}*}(\mathbf{x}) \varphi_{0,a}^{\text{KS}}(\mathbf{x}) f^{\text{Hxc}}[n_0](\mathbf{x}, \mathbf{x}', \Omega) \varphi_{0,i'}^{\text{KS}}(\mathbf{x}') \varphi_{0,a'}^{\text{KS}*}(\mathbf{x}').$$

The indices i/i' and a/a' run over all occupied and unoccupied Kohn-Sham states, respectively. This includes continuum states, and thus, in theory, this poses an infinite-dimensional eigenvalue problem. In practice, only a finite number of unoccupied states is taken into account.

Time Propagation

A different, arguably more direct, approach to calculating the linear-response of the system to an external potential is to actually apply a perturbation of the form $v_1^{\text{ext.}}(\mathbf{r}, \omega) = -r_j \kappa(\omega)$ at time $t > 0$ and to propagate in time the system numerically according to Equation (13) [23]. The linear-response of the dipole moment $\langle \hat{X} \rangle_1(\omega)$ can then be expressed as

$$\langle \hat{X}_i \rangle_1(\omega) = \int d^4x r_i n_1(\mathbf{x}, \omega).$$

The ‘‘polarizability’’ tensor α_{ij} of the system is defined as

$$\alpha_{ij} = \frac{\langle \hat{X}_i \rangle_1(\omega)}{\kappa(\omega)}.$$

The full tensor α_{ij} is obtained by re-running the simulation for different excitation direction r_j , or using any symmetries the system might have [23]. It can be shown, that the absorption cross-section tensor $\sigma(\omega)$ can be calculated as imaginary part of α [23]

$$\sigma(\omega) = \frac{4\pi\omega}{c} \text{Im}\{\alpha(\omega)\}.$$

2.2.3 Description of Photoemission in TD-DFT

An incident light field of sufficient energy $\hbar\omega$ is capable of exciting a previously bound electron from a surface or molecule into an unbound state in the vacuum. In this work we will exclusively focus on simulating the photoemission process for single, isolated molecules in the gas-phase. The momentum \mathbf{p} of the freed electron is fixed by the energy conservation during the emission process

$$\begin{aligned} |\mathbf{p}| &= \sqrt{2E_{\text{kin}}} \\ E_{\text{kin}} &= \omega - |E_b|. \end{aligned} \tag{19}$$

We can describe the photoemission spectrum $\mathcal{P}(\mathbf{p})$ of a molecule, i.e., the probability to measure an electron with momentum \mathbf{p} at the detector surface, normalized to the total number of escaped electron $N_{\text{esc.}}$, as a function $\mathcal{P}(\theta, \phi, E_{\text{kin}})$ of the spherical coordinates θ , ϕ and the kinetic energy E_{kin} of the escaping electron. The experimental technique called “angle-resolved photoemission spectroscopy” (ARPES) is capable of measuring the angular dependence of the photoemission data. Note that in principle also spin resolution can be achieved with spin-sensitive detectors [24], however, this is outside the scope of this work and will not be considered in the following theoretical description either.

The benefit of employing TD-DFT for the description of photoemission is, that it allows for a real-time formulation of arbitrary time-dependent external fields in both shape and strength. As a particularly attractive application, also the simulation of “pump-probe” photoemission experiments becomes possible. In a pump-probe setup, first a low energy pulse, the so-called “pump” pulse, excites electrons in the molecule to higher energy levels. The second pulse, now called “probe” pulse, then releases electrons from both the excited states and lower lying states into the vacuum according to Equation (19). By varying the time delay Δt between the two pulses, the temporal evolution of the excitation dynamics can be studied, both, in experiment and in the TD-DFT simulation.

There have been several attempts to simulate the angle-resolved photoemission current within the framework of TD-DFT [25, 26, 27]. This work uses the “time-dependent surface flux method” (t-SURFF), first proposed for atoms by Tao and Scrinzi [28], later formulated in the framework of TD-DFT and implemented into the real-space real-time simulation code “Octopus” (see Chapter 3.1.1) by Wopperer et al. [29] and further extended to semi-periodic systems by De Giovannini et al. [8] (t-SURFFP).

In TD-DFT the light field is treated classically. We can, therefore, modify

the Kohn-Sham Hamiltonian (13) in a minimal-coupling approach by coupling the vector potential $\mathbf{A}(t)$ to the momentum operator using the velocity gauge

$$\hat{H}^{\text{KS}} = \frac{1}{2} [i\nabla - \mathbf{A}(t)]^2 + \hat{v}^{\text{KS}} [n, \Phi_0] (\mathbf{r}, t).$$

Note that the electric field of the incident light beam is related to the vector potential by $\mathbf{E}(t) = \partial_t \mathbf{A}(t)$. The typical wavelength used in pump-probe experiments ($> 100 \text{ \AA}$) is much larger than the typical dimension of a single molecule ($\approx 10 \text{ \AA}$). This justifies our use of the dipole approximation $\mathbf{A}(\mathbf{r}, t) = \mathbf{A}(t)$ and the absence of a magnetic field component $\mathbf{B}(t) = \nabla \times \mathbf{A}(t) = 0$.

In order to compute the photocurrent using the t-SURFF method, the simulation box is split into a region A close to the molecule and an adjacent region B far enough from the molecule. We assume that the electronic structure dynamics can be described with two separate Hamiltonians \hat{H}^A and \hat{H}^B

$$\hat{H} = \begin{cases} \hat{H}^A & \mathbf{r} \in A \\ \hat{H}^B & \mathbf{r} \in B \end{cases} \quad (20)$$

In particular, the electrons in the outer region B will resemble free electrons which are still under the influence of the incident light $\mathbf{A}(t)$

$$\hat{H}^B = \hat{H}^V = \frac{1}{2} [i\nabla - \mathbf{A}(t)]^2.$$

Thus, the electrons in region B can also be described by the exactly solvable Volkov Hamiltonian \hat{H}^V [30], whose solutions $\chi_{\mathbf{p}}(\mathbf{r}, t)$ are plane waves with a time- and momentum-dependent phase factor $\Phi(\mathbf{p}, t)$

$$\chi_{\mathbf{p}}(\mathbf{r}, t) = \frac{1}{\sqrt{V}} e^{-i\Phi(\mathbf{p}, t)} e^{i\mathbf{p}\mathbf{r}}$$

$$\Phi(\mathbf{p}, t) = \frac{1}{2} \int_0^t [\mathbf{p} + \mathbf{A}(\tau)]^2 d\tau.$$

Because they form a complete and orthogonal basis set, the Kohn-Sham orbitals $\varphi_i^{\text{KS}}(\mathbf{r})$ can be expanded in terms of $\chi_{\mathbf{p}}(\mathbf{r}, t)$

$$\varphi_i^{\text{KS}}(\mathbf{r}, t) = \int b_i(\mathbf{p}) \chi_{\mathbf{p}}(\mathbf{r}, t) d^3p. \quad (21)$$

Using the continuity Equation (11), the total number freed electrons $N_{\text{esc.}}$ at the time T

$$N_{\text{esc.}}(T) = \sum_{i=1}^N \int |b_i(\mathbf{p})|^2 d^3p \quad (22)$$

is connected to the flux of the charge density $\mathbf{j}(\mathbf{r}, t)$ through the boundary surface S between the region A and B

$$N_{\text{esc.}}(T) = - \int_0^T d\tau \oint_S d\mathbf{s} \cdot \mathbf{j}(\mathbf{r}, \tau). \quad (23)$$

For the Kohn-Sham system we can express the charge density as a sum of expectation values of the hermitian, single-particle current-density operators $\hat{\mathbf{j}}_i(\mathbf{r})$

$$\mathbf{j}(\mathbf{r}, t) = \sum_{i=1}^N \langle \varphi_i^{\text{KS}}(\mathbf{r}, t) | \hat{\mathbf{j}}_i(\mathbf{r}) | \varphi_i^{\text{KS}}(\mathbf{r}, t) \rangle, \quad (24)$$

whose explicit form is the i th term of Equation (7) after a minimal-coupling substitution $\nabla_i \rightarrow \nabla_i + i\mathbf{A}(t)$. We plug (24) into Equation (23) and expand the dual vector $\langle \varphi_i^{\text{KS}}(\mathbf{r}, t) |$ in the Volkov basis (21)

$$N_{\text{esc.}}(T) = - \sum_{i=1}^N \int_0^T d\tau \oint_S d\mathbf{s} \int d^3p \cdot b_i^*(\mathbf{p}) \langle \chi_{\mathbf{p}}(\mathbf{r}, \tau) | \hat{\mathbf{j}}_i(\mathbf{r}) | \varphi_i^{\text{KS}}(\mathbf{r}, \tau) \rangle. \quad (25)$$

Comparing Equation (22) and Equation (25), we can give an explicit form for the Volkov state expansion coefficients

$$b_i(\mathbf{p}) = - \int_0^T d\tau \oint_S d\mathbf{s} \langle \chi_{\mathbf{p}}(\mathbf{r}, \tau) | \hat{\mathbf{j}}_i(\mathbf{r}) | \varphi_i^{\text{KS}}(\mathbf{r}, \tau) \rangle.$$

The validity of this result depends on the assumption that the freed electrons are spatially well separated from the bound electrons. Therefore, the distance between the surface detector and the spatially localized bound electron density has to be sufficiently large.

2.2.4 Ehrenfest Dynamics

In Chapter 2.1.1 we have discussed Born-Oppenheimer dynamics, a way to calculate the force on the nuclei in a not explicitly time-dependent electron density $n(\mathbf{r})$. There, the time-dependence in the nuclear motion arises from the Hellman-Feynman forces calculated from static ground state densities obtained from self-consistent DFT calculations. In TD-DFT, the electron density has, however, an additional explicit time-dependence $n = n(\mathbf{r}, t)$ due to an explicitly time-dependent external potential $\hat{v}^{\text{ext.}}(\mathbf{r}, t)$, e.g., due to a light field. In this case, the force \mathbf{F}_J on the core J can be calculated as [31]

$$\mathbf{F}_J(t) = - \int d^3r n(\mathbf{r}, t) \frac{\partial}{\partial \mathbf{R}_J} \hat{v}^{\text{ext.}}(\mathbf{r}, t).$$

This equation couples to the nuclear part of the external potential in Equation (14) and, therefore, has to be reevaluated at each time step.

2.3 Rabi Oscillation

As a result of a converged DFT groundstate calculation, the Kohn-Sham orbitals satisfy, by design, the time-independent Schrödinger equation

$$\hat{H}_0 |\varphi_n(\mathbf{r})\rangle = E_n |\varphi_n(\mathbf{r})\rangle$$

When adding a time-dependent sinusoidal perturbation, $\hat{H} = \hat{H}_0 + \hat{H}'$, with a frequency close to a resonant frequency $\omega \approx \omega_0 = |E_m - E_n|$ the system will undergo stimulated emission [32]. We assume, as is the case for the molecule ANBP (see Figure 1), that the two energy levels in question are non-degenerate. For the purpose of calculating the time-dependent excited state occupation, this allows us to treat the system as a two-level system. It is important to understand that although these two levels can be complicated in nature, for the response to the periodic field this complexity is neither relevant nor apparent. Treating the light field classically the entire system is described by the minimal coupling Hamiltonian [33]

$$\hat{H} |\Psi(\mathbf{r}, t)\rangle = \frac{1}{2} \left[\left(\hat{\mathbf{p}} - q\hat{\mathbf{A}}(\mathbf{r}, t) \right)^2 + q\hat{\Phi}(\mathbf{r}, t) \right] |\Psi(\mathbf{r}, t)\rangle \quad (26)$$

where q is the charge of the electron which we keep explicit for now and $\hat{\mathbf{A}}(\mathbf{r}, t)$ and $\hat{\Phi}(\mathbf{r}, t)$ are the vector and scalar potentials, respectively. We will employ the dipole approximation $\hat{\mathbf{A}}(\mathbf{r}, t) = \hat{\mathbf{A}}(t)$, i.e. neglect the spatial dependence in the electric field (see Chapter 2.2.3). It still leaves us with a gauge freedom for which we choose a special Coulomb gauge transformation $\hat{\chi}(t) = -\hat{\mathbf{x}}\hat{\mathbf{A}}'(t)$ called ‘‘Göppert-Mayer gauge’’ [34] or sometimes called ‘‘length gauge’’

$$\begin{aligned} \hat{\mathbf{A}}(t) &:= \hat{\mathbf{A}}'(t) + \nabla\hat{\chi}(t) = 0 \\ q\hat{\Phi}(\mathbf{r}, t) &:= \hat{\Phi}'(\mathbf{r}, t) - \partial_t\hat{\chi}(t) = q\hat{\mathbf{x}}\hat{\mathbf{E}}(t), \end{aligned}$$

where $\hat{\mathbf{E}}(t) = \mathbf{E}_0 \cos\omega t$ is the electric field with an amplitude of \mathbf{E}_0 in the dipole approximation.

Excited State Occupation

In order to solve Equation (26), we make an ansatz for the wavefunction of the full system as a time-dependent superposition of the two unperturbed levels

$$|\Psi(\mathbf{r}, t)\rangle = c_1(t) e^{-iE_1 t} |\varphi_1(\mathbf{r})\rangle + c_2(t) e^{-iE_2 t} |\varphi_2(\mathbf{r})\rangle.$$

Note that we explicitly kept the time-dependent phase factor resulting from the time-dependent Schrödinger equation for the unperturbed system. The absolute square of the coefficients $|c_{1/2}(t)|^2$ then can be interpreted as the occupation of the two levels respectively. Inserting this ansatz into the time-dependent Schrödinger equation results in a coupled system of differential equations for the coefficients

$$\begin{aligned} \dot{c}_1(t) &= -i c_2(t) e^{-i\omega_0 t} H'_{12} \\ \dot{c}_2(t) &= -i c_1(t) e^{i\omega_0 t} H'_{21}. \end{aligned} \quad (27)$$

Here, we have introduced the matrix elements

$$\begin{aligned} H'_{12} &= \langle \varphi_1(\mathbf{r}) | \hat{H}' | \varphi_2(\mathbf{r}) \rangle \\ &= q \langle \varphi_1(\mathbf{r}) | \hat{\mathbf{x}} | \varphi_2(\mathbf{r}) \rangle \mathbf{E}_0 \cos \omega t \\ &= \mathbf{d}_{12} \mathbf{E}_0 \cos \omega t \\ &= H'_{21} \end{aligned} \quad (28)$$

where \mathbf{d}_{12} is the transition dipole moment. To arrive at Equation (27) we have neglected the diagonal elements of the perturbation Hamiltonian [35]. For the solution of Equation (27) we could assume a weak field and expand the solution in terms of orders of \mathbf{E}_0 [35]. However, this means the system would be residing in the groundstate mostly. Therefore, we will assume instead a near-resonant, but not necessarily weak, driving field $|\delta| := |\omega - \omega_0| \ll \omega + \omega_0$. Rewriting the cosine in Equation (28) in terms of exponentials yields

$$\dot{c}_2(t) = -i \frac{\Omega}{2} c_1(t) [e^{-i(\omega - \omega_0)t} + e^{i(\omega + \omega_0)t}], \quad (29)$$

where we have introduced the ‘‘Rabi frequency’’ $\Omega = \mathbf{d}_{12} \mathbf{E}_0$. Because of the (near) resonance condition we can neglect the fast oscillating second term in Equation (29), which is called ‘‘rotating wave approximation’’ [36]. We can then solve the system of differential Equations (27) analytically leading to

$$\begin{aligned} c_1(t) &= e^{-i\frac{\delta t}{2}} \left[\cos \frac{\Omega_R}{2} t - i \frac{\delta}{\Omega_R} \sin \frac{\Omega_R}{2} t \right] \\ c_2(t) &= -i \frac{\Omega}{\Omega_R} e^{i\frac{\delta t}{2}} \sin \frac{\Omega_R}{2} t, \end{aligned}$$

where $\Omega_R := \sqrt{\Omega^2 + \delta^2}$ denotes the ‘‘Rabi flopping frequency’’. The occupation of the excited state

$$|c_2(t)|^2 = \left[\frac{\Omega}{\Omega_R} \sin \frac{\Omega_R}{2} t \right]^2 \quad (30)$$

shows an oscillation between 0 and $[\Omega/\Omega_R]^2$ with the Rabi flopping frequency. This phenomenon can be interpreted as the process of stimulated emission. In the first half cycle, the system takes energy from the electric field. When switching off the light field there after a so-called ‘‘ π -pulse’’ [37], the system is maximally excited and will, not taking any decoherence effects into account, stay there indefinitely. However, when continuously applying the perturbation, the system will relax back to the initial state because in the second half cycle the system emits a photon with the same energy as the laser pulse, provided there is perfect resonance.

Dipole Moment

Finally, we also want to calculate the expectation value of the dipole moment. This will be important later on for the interpretation of the simulation results. From the definition [36]

$$\mathbf{d} := \langle \Psi(\mathbf{r}, t) | \hat{\mathbf{d}} | \Psi(\mathbf{r}, t) \rangle = \mathbf{d}_{12} \cdot [c_1^*(t) c_2(t) e^{-i\omega_0 t} + c_1(t) c_2^*(t) e^{i\omega_0 t}]$$

we get

$$\mathbf{d} := \mathbf{d}_{12} \Omega \left[\frac{\delta \cos \omega t \cos \Omega_R t}{\Omega_R^2} - \frac{\delta \cos \omega t}{\Omega_R^2} - \frac{\sin \omega t \sin \Omega_R t}{\Omega_R} \right] \quad (31)$$

where we used $\mathbf{d}_{21} = \mathbf{d}_{12}$ and $\mathbf{d}_{ii} = 0$. In Figure 3, the behaviour of the dipole moment as well as the ground- and excited state population for a two-level system is shown for a resonant, near-resonant and a non-resonant value of δ . For specific simulation parameters please refer to the figure caption. Moving away from resonance manifests itself in two clear observations: First, the lower energy level never fully depletes and the higher energy state never reaches full occupation. Second, the dipole moment for the fully resonant and non-resonant setup look very similar. It is, therefore, not possible to distinguish between them on the basis of the dipole moment alone [38]. Together with the excited state population we can, however, see a clear difference: the nodes in the dipole moment seen in the fully resonant state align alternately with the maxima respectively the minima of the excited state population. As can be seen in panel (b), every odd node broadens as we move away from resonance and eventually gives rise to a new maxima in the envelope of the

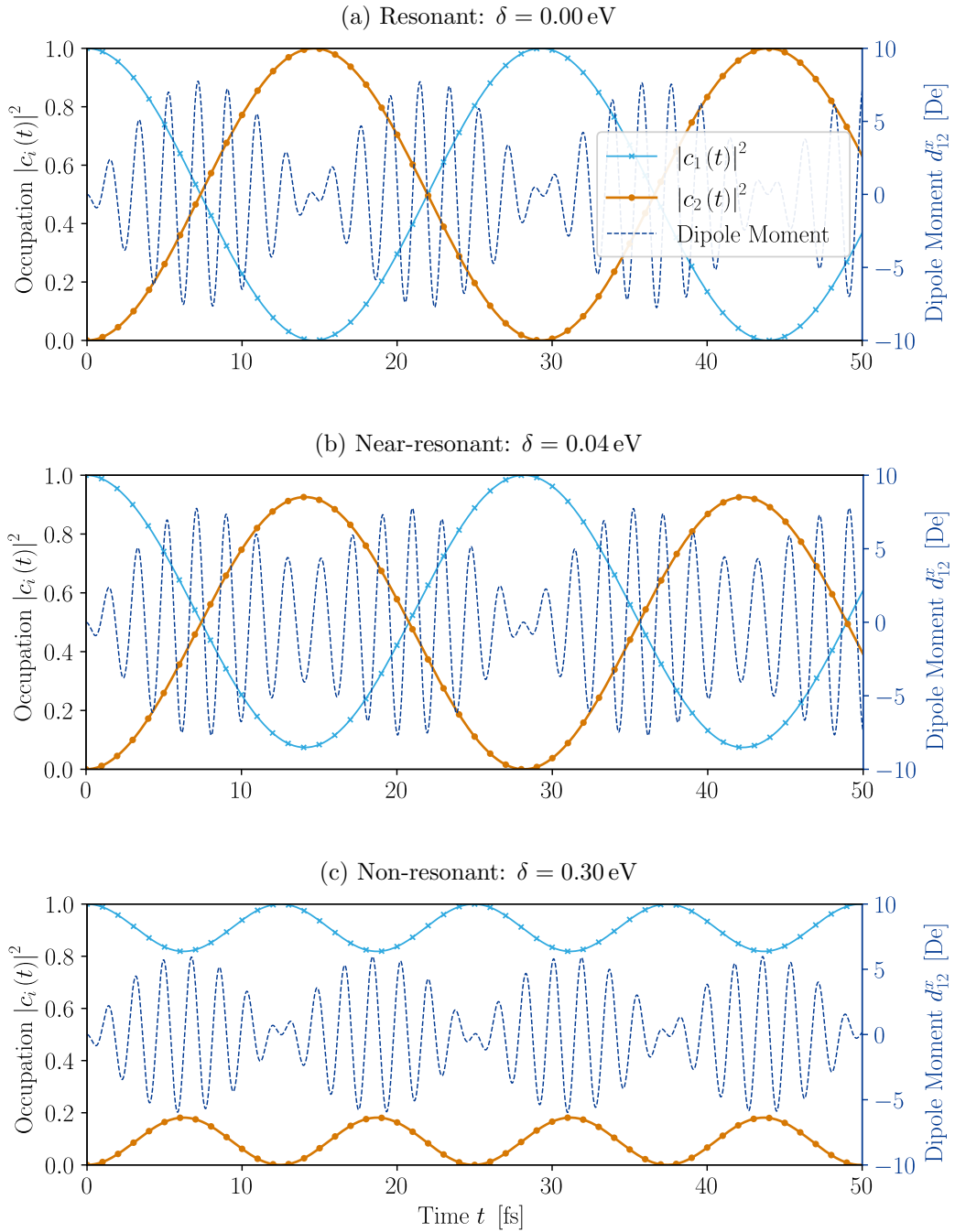


Figure 3: Simulation of the dipole moment d_{12}^x (dashed dark blue line; Eq. (31)), the groundstate population $|c_1(t)|^2$ (solid light blue line with crosses) and the excited state population $|c_2(t)|^2$ (solid orange line with circles; Eq. (30)) for different values of δ . Other relevant parameters used in this figures are: $\Omega = 0.14$ eV, $\omega_0 = 2.17$ eV, $d_{12}^x = 7.76$ De.

dipole moment. This has the consequence that now all the maxima in the dipole moment align with the maxima in the excited state population, odd and even. These two observations give us a clear way to distinguish possible off-resonant behaviour in the Rabi cycle later on.

2.3.1 Mollow-(like) Triplets

In fluorescence spectra of a resonantly driven two-level system one can observe a splitting of the emission peaks in the energy domain into three distinct peaks separated from the central emission line by $\pm\Omega_R$ [33]. This phenomena is called ‘‘Mollow Triplet’’ after the physicist who first theoretically described them in 1969 [39]. The derivation is a bit more involved, however, it can be understood fairly easily and intuitively [32]: The emission of light by an electron can only occur via de-relaxation from the excited state back to ground state. The emitted light will then carry the energy $\omega = \omega_0$. Thus, using Eq. (30), the emitted field will be

$$E^{\text{emitt.}}(t) \approx E_0^{\text{emitt.}} \cos \omega_0 t \sin \frac{\Omega_R}{2} t$$

which after Fourier transformation to the energy domain yields

$$E^{\text{emitt.}}(\nu) \approx E_0^{\text{emitt.}} \sqrt{\frac{\pi}{8}} \left[\frac{1}{4} \delta(\nu - \omega) + \frac{1}{4} \delta(\nu + \omega) - \delta(\nu - (\omega + \Omega_R)) \right. \\ \left. + \delta(\nu - (\Omega_R - \omega)) - \delta(\nu - (\omega - \Omega_R)) - \delta(\nu - (-\omega - \Omega_R)) \right]$$

The second, fourth and sixth term can be disregarded as all three quantities ν , ω and Ω_R have to positive. Thus we expect three peaks at $\nu = \omega$ and $\nu = \omega \pm \Omega_R$.

A different but apparently very similar observation will be possible in the TD-DFT simulation data later on (and in fact can already be seen here [40]): Both, the dipole moment as well as the excited state population show a similar splitting in the energy domain again by the term $\pm\Omega_R$. For the dipole moment, this is not too surprising as it can already be seen from Figure 3 a) and c) by the same argument as before: It oscillates with a term proportional to the laser frequency multiplied with an envelope function resembling a \sin^2 function with a periodicity identical to the occupation, i.e. Ω_R .

Understanding the analogous effect for the occupation is, however, not at all obvious from Eq. (30). Using the result (30) there is only a single (positive) frequency at Ω_R . This is a consequence of the rotating wave approximation

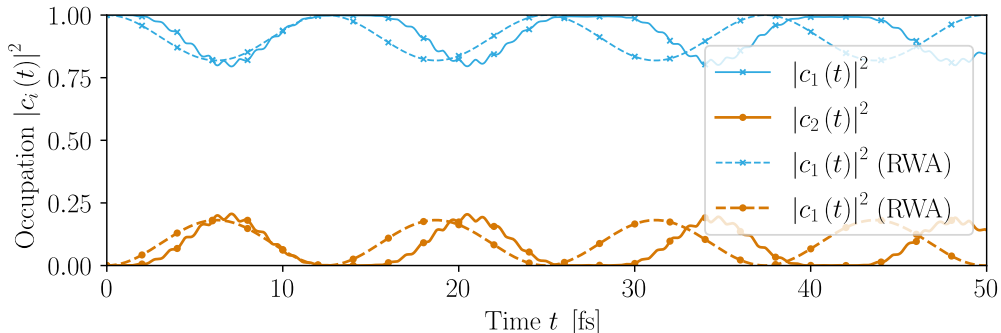


Figure 4: Numerical integration of Equations (27) without the rotating wave approximation using the Runge-Kutta algorithm of 4th order (solid lines). Solutions with the rotating wave approximation as comparison (dashed lines). The simulation parameters are identical to Figure 3c, namely: $\delta = 0.30$ eV, $\Omega = 0.14$ eV, $\omega_0 = 2.17$ eV and $d_{12}^x = 7.76$ De.

we used to obtain this results. In fact, going back to Eq. (27) and solving the coupled system of differential equations numerically will yield the same Mollow-like triplet structure for the excited state population as well. It is noticeable by a fast oscillation with ω on top of the already depicted slower oscillation Ω_R (see Figure 4).² In addition, we notice an increase in frequency using the RWA.

2.3.2 Failure of TD-DFT

When studying the resonant pumping a molecular system between two non-degenerate levels in the framework of TD-DFT, the results do not fully replicate the analytically derived Rabi physics from Chapter 2.3. This shortcoming of TD-DFT has already been described in the literature for 1D toy models [37, 38]. Its origin still is, however, contested. It is claimed to be either of classical origin due an anharmonic potential [37] or an inherent issue of all mean-field theories and only solvable by giving up the adiabatic approximation of the xc-functional [38]. In this chapter the argument of the second position [38] and possible remedies [40] will be presented briefly.

²It splits into a triplet not a duplet because the square of a sine wave gives an additional identical negative frequency Ω_R shifted by the second oscillation ω into the positive domain.

Dynamical Detunement

The time-dependent Kohn-Sham Hamiltonian is given by the following expression

$$\hat{H}^s = \underbrace{\hat{T} + \hat{V}^{\text{nuc.}}}_{\hat{H}_0^s} + \overbrace{\hat{V}_0^{\text{xc}} + \hat{V}_{\text{dyn.}}^{\text{xc}}}^{\hat{V}^{\text{xc}}} + \hat{H}',$$

where \hat{T} , $\hat{V}^{\text{nuc.}}$ and \hat{V}^{xc} are the kinetic energy functional, the external potential functional resulting from the nuclei and the exchange-correlation functional, respectively. The last one we split into a static part \hat{V}_0^{xc} depending only on the electron density at $t = 0$ and a dynamic part $\hat{V}_{\text{dyn.}}^{\text{xc}}$ depending on the full history of electron density. \hat{H}' represents an external electromagnetic field interacting with the system. In matrix notation the Equations (27) take now the following form

$$\begin{pmatrix} \dot{c}_1(t) \\ \dot{c}_2(t) \end{pmatrix} = -i \begin{pmatrix} \langle \varphi_1 | \hat{V}_{\text{dyn.}}^{\text{xc}} | \varphi_1 \rangle & \langle \varphi_1 | \hat{V}_{\text{dyn.}}^{\text{xc}} | \varphi_2 \rangle + \hat{H}'_{12} \\ \langle \varphi_2 | \hat{V}_{\text{dyn.}}^{\text{xc}} | \varphi_1 \rangle + \hat{H}'_{21} & \langle \varphi_2 | \hat{V}_{\text{dyn.}}^{\text{xc}} | \varphi_2 \rangle \end{pmatrix} \times \begin{pmatrix} c_1(t) \\ c_2(t) \end{pmatrix}.$$

All four matrix elements have picked up an additional term $\langle \varphi_i | \hat{V}_{\text{dyn.}}^{\text{xc}} | \varphi_j \rangle$ depending implicitly on the time. They have been explicitly calculated for the adiabatic exact-exchange xc-functional AEXX in Ref. [38], where it is shown that these terms lead to a dynamical shift of the resonant frequency proportional to $c_2(t)$. This implicit time-dependence makes it impossible to drive the system resonantly for the duration of the whole Rabi cycle and manifests itself in an omnipresent detunement δ , which, in turn, prohibits a high percentage of excited level occupation.

Reference [38] argues that this shortcoming is an inherent consequence of all adiabatic mean-field theories (e.g. Hartree-Fock) and can only be fully lifted by inclusion of the full history of the xc-functional recovering the true form of the xc-functional.

Possible Remedies

In her doctoral thesis [40], Jokar investigated the influence of different types of static xc-functionals (ALDA, AEXX, ALDA-ADSIC and ALDA + full SIC) on the dynamical detunement of a 1D toy model with two electrons. She has found that for this Helium atom-like system in the singlet case, none of the studied functional shows resonant Rabi physics, with only a slight improvement going from ALDA ($|c_2(t)|^2 = 0.09\%$) to a more sophisticated one ($|c_2(t)|^2 \leq 0.15\%$). However, for the triplet case even ALDA achieves

an excited state population of $|c_2(t)|^2 = 0.43\%$ with an improvement up to $|c_2(t)|^2 = 0.84\%$ for the AEXX functional. Using an off-resonant frequency $\omega_{\text{best}} = 0.984\omega_{\text{l.r.}}$ close to the frequency $\omega_{\text{l.r.}}$, determined from a linear response calculation, leads again to an improvement in the excited state population ($|c_2(t)|^2 = 0.95\%$) and near-resonant behaviour.

Further simulations confirmed that the most important aspect is the number of electrons participating in the transition to the excited state, not the spin directions. Resonant Rabi oscillation and high excited state population was confirmed for a 1D three electron system (i.e. resembling Lithium) and for a 3D Helium atom in a triplet groundstate using HGH pseudo-potentials as well.

3 Results

3.1 Computational Setup

To obtain the results presented in this work, the two ab-initio electronic structure codes “Octopus” [41] and “GPAW” [42] have been employed on the “Vienna Scientific Cluster 3” (VSC-3). Both codes are free and open-source software packages publicly released under the GPLv3 license. In this chapter, we want to briefly present both codes and what they have been used for in this work. For example inputs demonstrating on how to use them in more detail, we refer to the Appendices A and B, respectively.

3.1.1 Octopus

Octopus [41, 43, 44] is a real-space, real-time ab-initio pseudo-potential time-dependent density functional theory code. All quantities, such as potentials and densities, are expanded on a regular mesh in real-space, and the simulations are performed in real-time [41]. In its current version 11.4, Octopus provides a number of different features, including groundstate DFT, linear response TD-DFT [45] in multiple different formalisms (Sternheimer [46], time-propagation [23] and Casida [22]; see Chapter 2.2.2), periodic and non-periodic boundary conditions in 1, 2 or 3 dimensions, absorbing boundary conditions [47], molecular dynamics (Car-Parrinello [48] and Ehrenfest [31]; see Chapter 2.2.4), as well as a large number of xc-functionals via the “LIBXC” library [49].

The software is written mostly in Fortran 90 and is highly parallelizable on both CPU and GPU using MPI and CUDA, respectively. Furthermore, although not optimized for the calculation of groundstate properties [41], Octopus performs well on a large number of processors and time-dependent calculations are highly parallelizable in individual Kohn-Sham states, grid domain and k -points for extended systems [50].

Octopus was the main code used for most simulations shown in this work, except for the initial geometry relaxation in the Born-Oppenheimer approach and some additional linear response calculations. In particular, Octopus was chosen for its implementation of the detection of photoelectrons [28] [41] with the t-SURFF method [29, 8] (see Chapter 2.2.3). The input is handled via a dedicated input file named `inp`, resembling a configuration file. For an example of such a file used to calculate the photoemission intensity, please see Appendix A.

Unless otherwise stated, all simulations in this work done with Octopus used

the pseudo-potential set by Hartwigsen-Goedecker-Hutter HGH [51] and the local density xc-correlation functional. The former was chosen due to some convergence issues in the self-consistency cycle for the groundstate calculations using the default standard set of pseudo-potentials provided by the software. The propagator scheme used for time-dependent calculations is the “approximated enforced time-reversal symmetry (aetrs)” [52].

3.1.2 GPAW

GPAW [42, 53] is Python module based on the “Atomic Simulation Environment” ASE [54, 55] implementing the projector-augmented wave method (PAW) [56, 57, 58] for (time-dependent) density functional theory. It can use both a localized (LCAO) and non-localized (plane wave) basis sets, as well as no basis set (real-space) [59] for the pseudo-wavefunction in periodic, non-periodic or mixed boundary conditions. The feature set in its current release 22.1.0 includes groundstate and time-dependent real-time DFT, linear-response TD-DFT, DFT+U [60], GW [61] and BSE [62].

Even though performance critical sections are implemented in C, the implementation of the main body of the software in Python makes GPAW a highly accessible electronic-structure code. Calculations can be parallelized over bands, k -points and real-space domains using MPI.

In this work, GPAW was mainly used for the relaxation of the geometry in a finite-difference scheme (real-space). Additionally, some optical responses in the linear regime have been calculated with GPAW. As GPAW is a Python module, the interaction with the program is structured like a Python script. An example script for a structure relaxation is added in Appendix B.

Note that in calculations done with GPAW, for all parameters not specifically mentioned, the default value provided by the software has been used. This includes the local density xc-functional and the corresponding projector-augmented wave set provided by GPAW (`gpaw-setups-0.9.20000.tar.gz`).

3.1.3 VSC-3

The “Vienna Scientific Cluster” VSC is a family (VSC-3, VSC-4 and VSC-5) of general-purpose supercomputers located in Vienna, Austria. The VSC-3 is the oldest currently (July 2022) still active of the three and was installed 2014 by ClusterVision. At the time of installation (November 2014), it employed 2020 nodes with two Intel Xeon E5-2650v2 processors each and ranked 85 worldwide in terms of speed. After an extension in 2018 (VSC-3+; additional 864 nodes with two Xeon E5-2660v2 each) its designated EOL is 2022. The

individual nodes come with either 64 GB or 256 GB memory and uses the scheduler SLURM. Access to the cluster was funded by the Austrian Science Fund (FWF) project I3731.

Table 1: Geometry of 4-Amino-4'-nitrobiphenyl as result of a Born-Oppenheimer relaxation procedure described in Chapter 2.1.1 and Chapter 3.2. Due to symmetry reasons, the molecule is completely planar and all z -coordinates are 0.000 Å.

Atom	x -Pos. [Å]	y -Pos. [Å]	Atom	x -Pos. [Å]	y -Pos. [Å]
C	-2.839	-1.204	H	-3.418	-2.132
C	-2.839	1.204	H	-3.418	2.132
C	-1.463	-1.195	H	-0.939	-2.154
C	-1.463	1.195	H	-0.939	2.154
C	1.469	-1.187	H	0.954	-2.151
C	1.469	1.187	H	0.954	2.151
C	2.845	-1.196	H	3.383	-2.149
C	2.845	1.196	H	3.383	2.149
C	-3.520	0.000	H	5.446	-0.870
C	-0.730	0.000	H	5.446	0.870
C	0.730	0.000	O	-5.534	-1.083
C	3.569	0.000	O	-5.534	1.083
N	-4.965	0.000	N	4.926	0.000

3.2 Geometry Optimization

The atomic structure of the molecule in question, 4-Amino-4'-nitrobiphenyl ANBP (see Figure 1), has been relaxed using GPAW in finite-difference mode, i.e. no basis set, with a grid spacing of 0.02 Å (see Table 1). The relaxation was done in a quasi-Newton scheme with a convergence criteria for the individual atomic forces of $< 0.02 \text{ eV } \text{Å}^{-1}$. As input geometry, a force-field calculation from the software Avogadro2 has been used and an additional 14 Å vacuum on each side has been added. From a stereochemical point of view, a twist around the central C-C bond could be expected. However, by not breaking the symmetry the molecule has been forced, intentionally, to remain planar. The reason is that, even though in this work only the gas-phase molecule has been studied, in an experiment the molecule would need to be adsorbed onto a surface, preventing this twist.

3.3 Optical Response

In order to induce near-resonant Rabi behaviour in the system, the laser frequency needs to be tuned to the resonance energy of the system. As discussed in Chapter 1, we are primarily interested in the HOMO-LUMO transition ($40 \rightarrow 41$) since it implies the intra-molecular charge transfer of interest. Please note, the number 40 for the HOMO arises due to the use of a pseudopotential, which excludes core-bound electrons from the counting. Because the energies of the unoccupied Kohn-Sham states cannot be directly identified with the eigenenergies of the fully-interacting system (Janak’s Theorem, Chapter 2.1), the energy difference $\Delta E_{40 \rightarrow 41} = 2.06$ eV from the groundstate calculation is only a crude first approximation to the transition energy. Much better results are obtained from linear-response calculations, as described in Chapter 2.2.2. To this end, three separate linear-response calculations have been performed, with different codes and or methods. Important to note is, that all three calculations explicitly exclude triplet excitations, i.e. they are “spin-restricted”.

Time-propagation (TP)

First, a full time-propagation of the system for a period $T = 13.16$ fs with a time step of $\Delta t = 0.0013$ fs after an initial Dirac δ -shaped kick with a wavevector $k_{\text{kick}} = 0.01 \text{ \AA}^{-1}$ has been performed with the software Octopus. The kick and the subsequent propagation have been repeated for each Cartesian direction to obtain the full polarizability tensor α_{ij} . The resulting optical absorption spectrum is plotted in Figure 5 (solid line). The mesh grid spacing $h = 0.17 \text{ \AA}$ and the box (“minimal”-shape) radius $R = 5 \text{ \AA}$ have been converged as individual separate parameters. As convergence criteria, the position and shape of the first absorption peak have been used, however, the spacing showed poor convergence behaviour (see Figure 6).

The resulting peak positions of the first two transitions are $E_1^{\text{TP}} = 2.70$ eV and $E_2^{\text{TP}} = 4.12$ eV, respectively. In the time-propagation scheme these peaks represent eigenmodes of the dipole moment of the system and no simple correspondence to transitions between Kohn-Sham states is possible. The first absorption peak, however, aligns well with the results of the Casida’s Equation and GPAW calculation discussed below.

Casida’s Equation

In Casida’s approach, the optical absorption spectrum is decomposed into transitions from electron-hole pairs, which allows an identification with state

transitions. For the linear-response calculation in the Casida formalism (see Equation (18)), 40 (+100 % of occupied states) additional, converged unoccupied states have been calculated with a spacing $h = 0.08 \text{ \AA}$ and a box radius $R = 6 \text{ \AA}$ (dashed line in Figure 5). The first two transition peaks are $E_1^C = 2.72 \text{ eV}$ and $E_2^C = 4.35 \text{ eV}$, respectively. A further decomposition of each peak into individual single-particle transitions (see Table 2) shows that the first peak is almost exclusively due to the HOMO \rightarrow LUMO transition we are interested in. Therefore, the pump laser frequency will be set close to $\omega \approx 2.7 \text{ eV}$ for subsequent simulations. This value has to be compared to the relative energy gap between the Kohn-Sham states $\Delta E_{40\rightarrow 41} = 2.1 \text{ eV}$, a difference likely to produce a noticeable detunement the subsequent Rabi (compare Figures 10 and 12.)

GPAW

As a third type of calculation to compare the previous results to, the linear-response has been calculated with GPAW (see dash-dotted line in Figure 5). GPAW uses an approach similar to Casida's equation as it starts from the Kohn-Sham density-density response χ^{KS} Equation (17) and obtains the fully interacting response χ by solving Dyson's equation

$$\chi = \chi^{\text{KS}} + \chi^{\text{KS}} f^{\text{Hxc}} \chi.$$

To this end, 50 additional unoccupied bands were considered, of which only the first 40 have been sufficiently converged and further used in the calculation. The box was a rectangular box with a vacuum of $R_v = 8 \text{ \AA}$ on each site and a grid spacing of $h = 0.24 \text{ \AA}$. Due to the construction via electron-hole pairs, it is again possible to decompose each absorption peak into individual single-particle transitions (see Table 2). This shows that, even though there is good agreement with the time-propagation for the first peak at $E_1^G = 2.67 \text{ eV}$, there is already a significant discrepancy of $E_2^G - E_2^{\text{TP}} = 0.20 \text{ eV}$ for the second peak at $E_2^G = 4.32 \text{ eV}$. This is not particularly relevant for this work, as this absorption peak is not dominated by the HOMO \rightarrow LUMO transition we are interested in (see Table 2).

Table 2: Relative contributions of the individual single-particle transitions for the first two major absorption peaks in Figure 5. Note that the HOMO is state 40, thus, the transition of interest HOMO→LUMO is denoted as 40 → 41. Any residual percentage arises from a large number of comparatively weak non-listed transitions or rounding.

Transitions	Absorption Peak 1 at ≈ 2.7 eV		Absorption Peak 2 at ≈ 4.3 eV	
	Octopus	GPAW	Octopus	GPAW
32 → 41	0.00	0.00	0.02	0.02
36 → 41	0.05	0.04	0.40	0.42
36 → 43	0.00	0.00	0.04	0.04
38 → 42	0.00	0.00	0.02	0.02
40 → 41	0.90	0.90	0.08	0.07
40 → 43	0.05	0.05	0.43	0.41

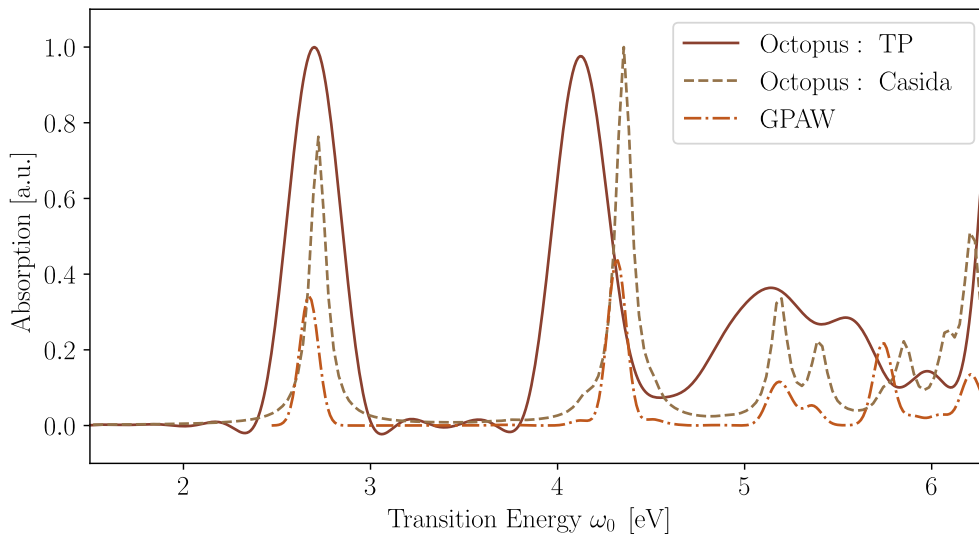


Figure 5: Absorption spectrum of gas phase ANBP obtained from three different linear-response calculations, two of which have been performed with Octopus and one with GPAW. The most important peak, consisting to a large degree of the HOMO-LUMO transition $\Delta E_{40 \rightarrow 41} = 2.06$ eV, occurs at $\omega_0 = 2.70$ eV for the time-propagation (solid line), at $\omega_0 = 2.72$ eV for the Casida formalism (dashed line) and at $\omega_0 = 2.67$ eV for the GPAW calculation (dash-dotted line), respectively. For details to each individual calculation please refer to Chapter 2.2.2.

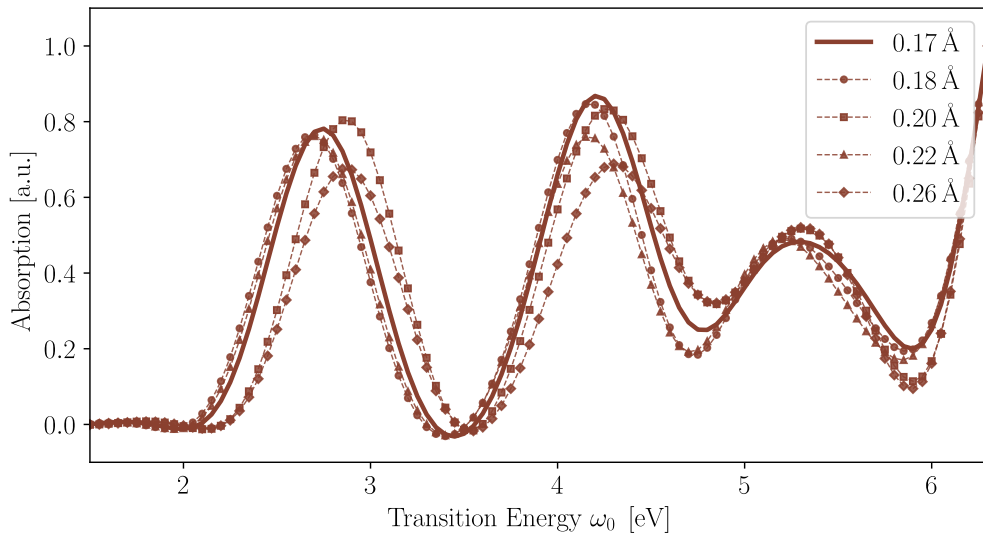


Figure 6: Absorption spectrum of gas phase ANBP obtained from a linear-response calculation in the time-propagation scheme with Octopus for different mesh grid spacings h . All calculations have been performed in a minimal box with radius $R = 3 \text{ \AA}$ for a propagation time of $T = 6.58 \text{ fs}$ with a time step of $\Delta t = 0.0013 \text{ fs}$. The solid line represents the finest grid, which has been used for the calculations in Figure 5 as well. However, there is no clear convergence towards a peak position or shape with the grid spacing.

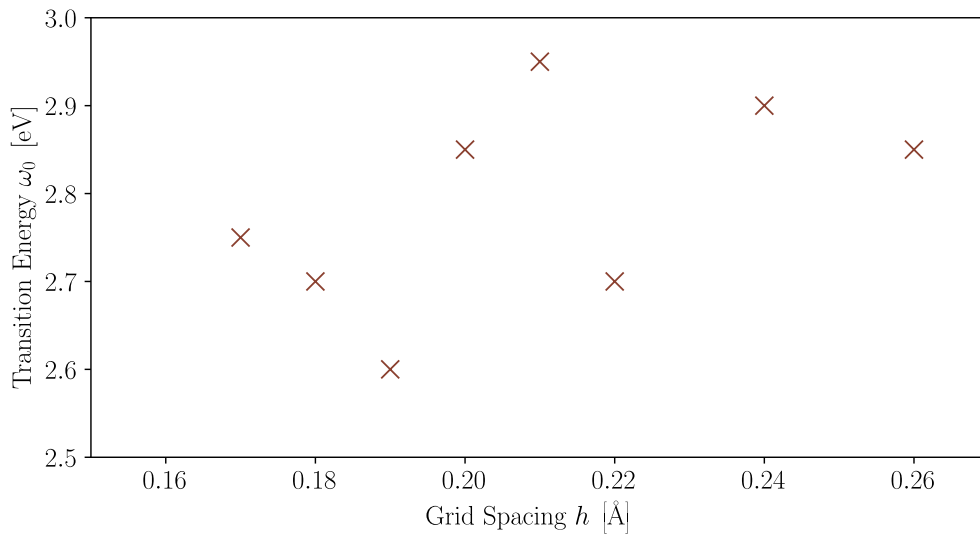


Figure 7: Transition energy ω_0 , i.e., the position of the first peak in the absorption spectrum, of gas phase ANBP for different grid spacings in a linear-response calculation in the time-propagation scheme.

3.4 LUMO Occupation

In this section we investigate, to which extent TD-DFT is capable of accounting for the Rabi physics described in Chapter 2.3. To this end, ANBP is excited by a pump pulse close to the resonant frequency determined in Chapter 3.3. First, however, we need to define a quantity which corresponds to the excited state population $|c_2(t)|^2$ (see Equation (30)) in the framework of TD-DFT. Propagating the groundstate KS-orbitals $\varphi_k^{\text{KS}}(\mathbf{x}, t)$ according to Equation (13) will not change the actual occupation of the individual orbitals, but the orbitals themselves. Therefore, we define

$$p_{i \rightarrow j}(t) := |\langle \varphi_i^{\text{KS}}(\mathbf{x}, t) | \varphi_j^{\text{KS}}(\mathbf{x}, 0) \rangle|^2,$$

the absolute square of the projection of the time-propagated orbital $\varphi_i^{\text{KS}}(\mathbf{r}, t)$ onto the groundstate of the orbital $\varphi_j^{\text{KS}}(\mathbf{r}, 0)$. In theory, if the HOMO orbital has been fully depleted by an excitation from the HOMO into the LUMO, this quantity will assume the values $p_{41 \rightarrow 40}(t) \neq p_{40 \rightarrow 41}(t) = 1$, $p_{40 \rightarrow 40}(t) = 1$ and $p_{41 \rightarrow 41}(t) = 1$, respectively. Of course, at the beginning of any simulation $p_{i \rightarrow i}(0) = 1$.

These time-dependent projections cannot be identified with the occupation number $|c_2(t)|^2$ directly, as it only describes the excitation from a single orbital to another single orbital. Multiply propagated orbitals can have a non-vanishing projection onto a common groundstate orbital. However, since we are interested in the two-level dynamics described in Chapter 2.3, this quantity suffices.

With the definition above, the HOMO→LUMO projection is studied for ANBP under the influence of a resonant laser frequency (see Figure 8). The pump pulse is tuned to the linear-response resonance frequency of the system showing a dominate contribution of said transition in the time-propagation scheme ($\omega = 2.70$ eV). The light field has a polarization along the long axis of molecule (x -direction) and its maximum field strength $E_0^x = 0.0017$ au $\hat{=} 0.874$ V nm $^{-1}$ is chosen such that the corresponding intensity $I = 10^{11}$ W cm $^{-2}$ is well within experimental reach [63]. To mitigate linear-response effects, the laser pulse is multiplied by a trapezoidal envelope function ramping the first and last $\tau = 2$ fs linearly. As mesh grid a minimal-type box of radius $R = 5$ Å and spacing $h = 0.18$ Å is used. The resulting projections HOMO→LUMO and HOMO→HOMO show, compared to Figure 4, two full cycles of a detuned Rabi-like oscillation. As is to be expected, the oscillation of both projections evolve with the same frequency, suggesting a time-dependent depletion of the HOMO by excitation into the LUMO in the first half of the Rabi cycle ($t \leq 8.8$ fs) followed by a de-excitation back to the HOMO

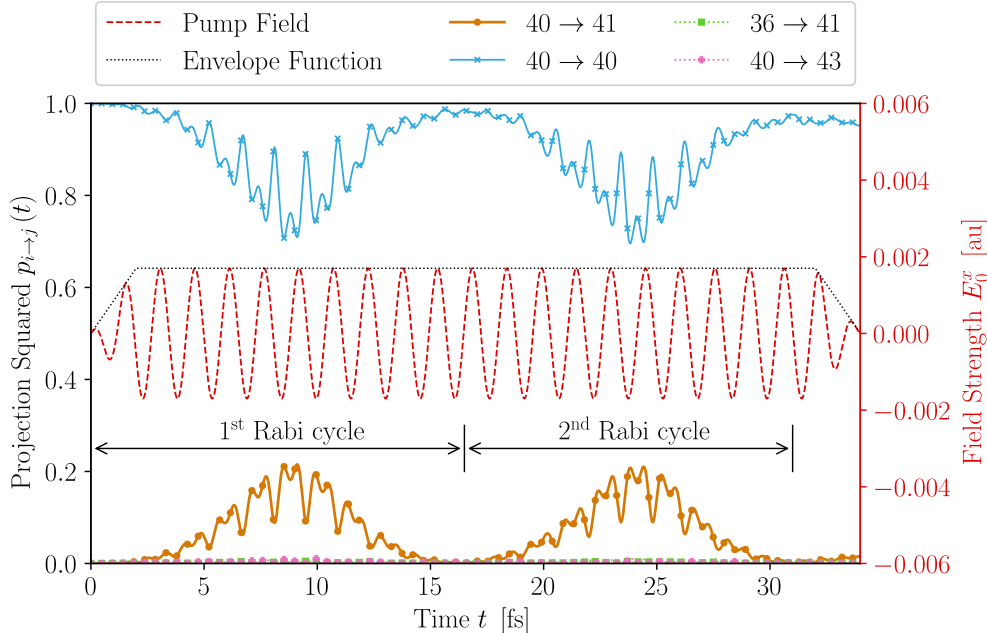


Figure 8: Time-dependent Kohn-Sham state projections (lines with markers) in ANBP under excitation by an resonant pump field. The laser (red dashed line) has a frequency $\omega = 2.70$ eV and a maximum electric field strength of $E_0^x = 0.0017$ au along the molecular axis (x -axis). The pulse is covered by an envelope function (black dotted line) ramping the intensity linearly for the first and last $\tau = 2$ fs.

for the second half ($8.8 \text{ fs} \leq t \leq 16.5 \text{ fs}$). Neither of the other two transitions (HOMO-4 \rightarrow LUMO and HOMO \rightarrow LUMO+2) predicted by the linear-response calculation (see Table 2) show any significant excitation. However, at $t = 8.53$ fs the HOMO displays a larger depletion of $p_{40 \rightarrow 40} = 0.71$ than there is excitation into the LUMO $p_{40 \rightarrow 41} = 0.21$, suggesting an additional transition from the HOMO into a different state. Most notably, even though a perfectly resonantly tuned laser frequency has been chosen, the Rabi oscillations appear to be highly detuned with a maximum HOMO-LUMO excitation of $p_{40 \rightarrow 41} = 0.22$. Comparing to Figure 3c, this is even more obvious looking at the dipole moment of the system Figure 9, where the peaks of the dipole moment envelope function align with the peaks of in LUMO occupation, which is characteristic for detuned Rabi physics.

From the linear-response calculation in the Casida formalism (see Chapter 3.3), we also get the transition dipole moment in x -direction for the

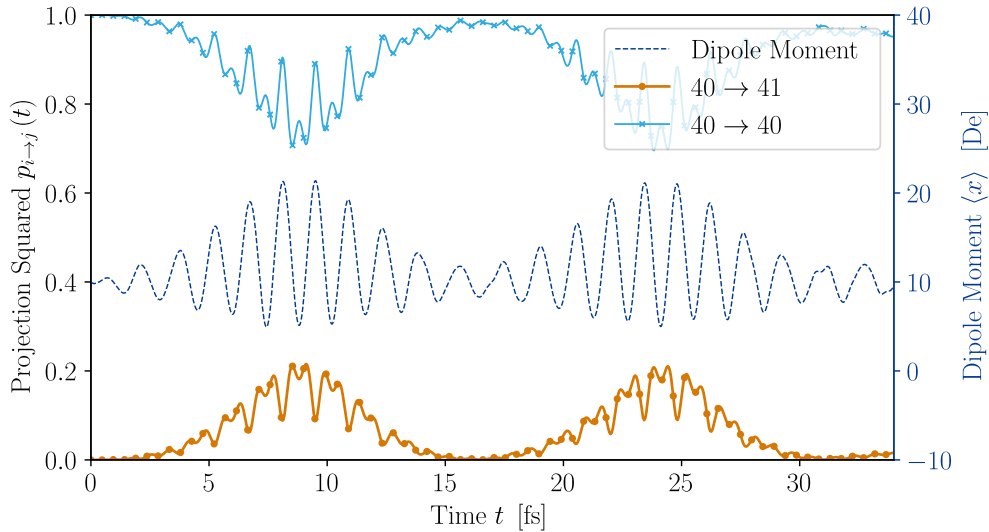


Figure 9: Identical calculation to Figure 8 but instead of the laser the dipole moment in x -direction $\langle x \rangle$ (dashed blue) line is shown. The peaks in the envelope of the dipole moment align with the peaks the envelope of the LUMO excitation, characteristic for detuned Rabi oscillation (see Figure 3c).

absorption peak $d_{12}^x = 6.20$ De. For the laser pulse used here, this results in a theoretical Rabi frequency $\Omega_{\text{theo.}} = d_{12}^x \cdot E_0^x = 0.027 \text{ fs}^{-1}$ compared to the TD-DFT simulation $\Omega = 1/T = 0.06 \text{ fs}^{-1}$, where $T = 16.50$ fs is the minimum HOMO \rightarrow HOMO projection after the first Rabi cycle.

Extended Time Propagation

As we have seen in the previous chapter, the Rabi frequency extracted from the TD-DFT time-propagation of the HOMO \rightarrow LUMO projection differs from the theoretical Rabi frequency by more than a factor of two. For a more accurate determination of the simulated oscillation frequencies, a similar calculation to the previous one has been performed with a total simulation period of $T = 200$ fs (see Figure 10). Additionally, this simulation setup differs from the previous one in a shallower slope $\tau = 5$ fs and a finer grid spacing $h = 0.15$ Å.

From Figure 10, we see that the Rabi oscillation starts to break down after the first couple of cycles. Accordingly, the maximum HOMO \rightarrow LUMO excitation in the system decreases already after the first cycle. The latter can be understood with our findings from Figure 8, where we noted that the HOMO depletion in every cycle is greater than the amount of electrons being

promoted to the LUMO from the HOMO. This suggests at least one more transition out of the HOMO and, as can be seen in the HOMO→HOMO projection in Figure 8, means that the HOMO does not revert back to its groundstate completely after each cycle. The reduced HOMO occupation at the start of the next cycle would explain the steady decrease in maximum HOMO→LUMO projection observed in Figure 10. This could also be a possible reason for the breakdown of the oscillation after multiple cycles.

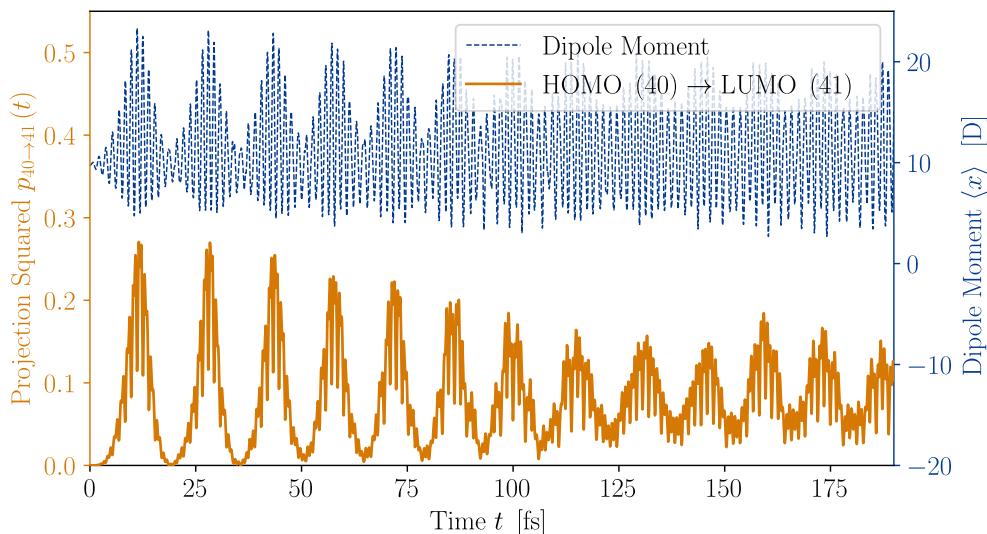


Figure 10: Calculation identical to Figure 8, except for a finer grid of $h = 0.15 \text{ \AA}$, for an extended period of time showing the evolution of the oscillation over multiple distinct Rabi cycles.

The spectral density $|\mathcal{F}(f)|^2$ of the resulting LUMO excitation $p_{40 \rightarrow 41}$ and dipole moment $\langle x \rangle$ as a function of frequency can be seen in Figure 11. The frequency resolution is $\Delta f = 1/T = 0.005 \text{ fs}^{-1}$, where $T = 200 \text{ fs}$ is the total simulation duration. The first large peak at $\Omega_{\text{sim.}} = 0.068 \text{ fs}^{-1}$ is close to the value of the Rabi oscillation found in Figure 8. It differs significantly from the theoretical value (shown with a dotted black line) of $\Omega_{\text{theo.}} = 0.027 \text{ fs}^{-1}$ obtained from the transition dipole moment, a result of the linear-response calculation, and the electric field strength. The most prominent peak in the dipole moment $\langle x \rangle$ at $f = 0.653 \text{ fs}^{-1}$ is directly related to the pump pulse, with an energy of $\omega = 2.70 \text{ eV} \hat{=} 0.653 \text{ fs}^{-1}$. As was discussed in Chapter 2.3.1, it is accompanied by two side peaks with a frequency difference of $\Delta f = \pm \Omega_{\text{sim.}}$, the observed Rabi frequency. At twice the laser frequency

$f = 1.374 \pm 0.068 \text{ fs}^{-1}$ the Mollow-like triplet repeats for the projection only, showing a second order harmonic behaviour. Even though ANBP has no inversion symmetry, the second order harmonic for dipole moment is still suppressed [36].

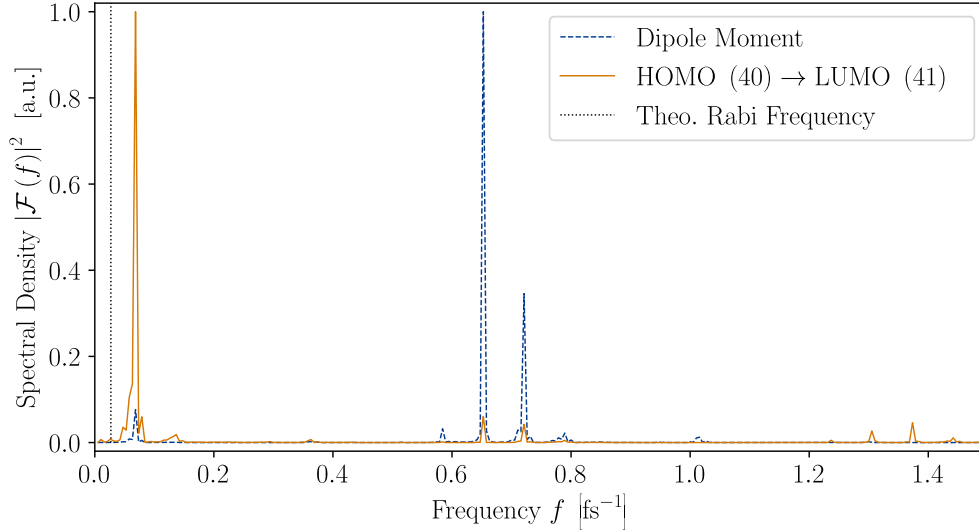


Figure 11: Spectral density of the HOMO→LUMO transition $p_{40 \rightarrow 41}$ (solid orange line) and dipole moment $\langle x \rangle$ (dashed blue line) from Figure 10. The black dotted line shows the theoretical value for the Rabi physics.

The extended time simulation shown in Figure 10 has been repeated for a pump pulse not tuned to the absorption peak at $\omega = 2.70 \text{ eV}$ but to the direct energy gap between the groundstate HOMO and LUMO orbitals at $\Delta E_{40 \rightarrow 41} = 2.06 \text{ eV}$. As can be seen in Figure 12, this drastically decreases the excitation from the HOMO into the LUMO and shows an even more detuned Rabi physics than what was observed before. This, therefore, can not explain the overall detunement found.

Dependence on Field Strength

In order to investigate the influence of the field strength on the Rabi physics, the calculation described in the Chapter 3.4 has been repeated for $E_0^x = 0.0017 \text{ au}/1.5 = 0.00113 \text{ au} \hat{=} 0.581 \text{ V nm}^{-1}$ and $E_0^x = 0.0017 \text{ au} \cdot 1.5 = 0.00255 \text{ au} \hat{=} 1.311 \text{ V nm}^{-1}$, with all other parameters identical. The resulting time-dependent HOMO→LUMO projection $p_{40 \rightarrow 41}$ can be seen in Figure 13, and the period and height of the first peak as a function of the

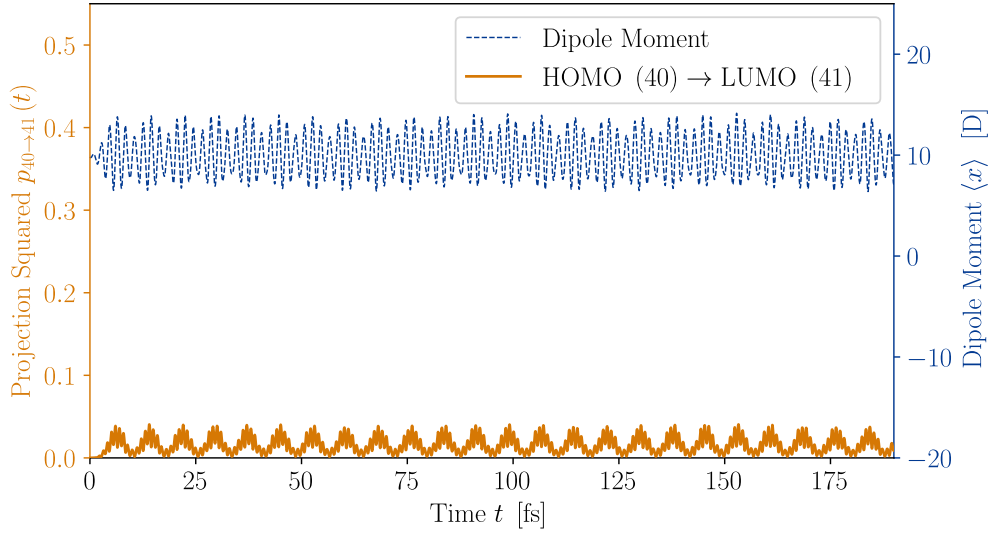


Figure 12: Calculation identical to Figure 10 but with an pump pulse of $\omega = \Delta E_{40 \rightarrow 41} = 2.06$ eV, the energy gap between the groundstate LUMO and HOMO state.

field strength in Figure 14. From Equation (30), we expect an inverse linear

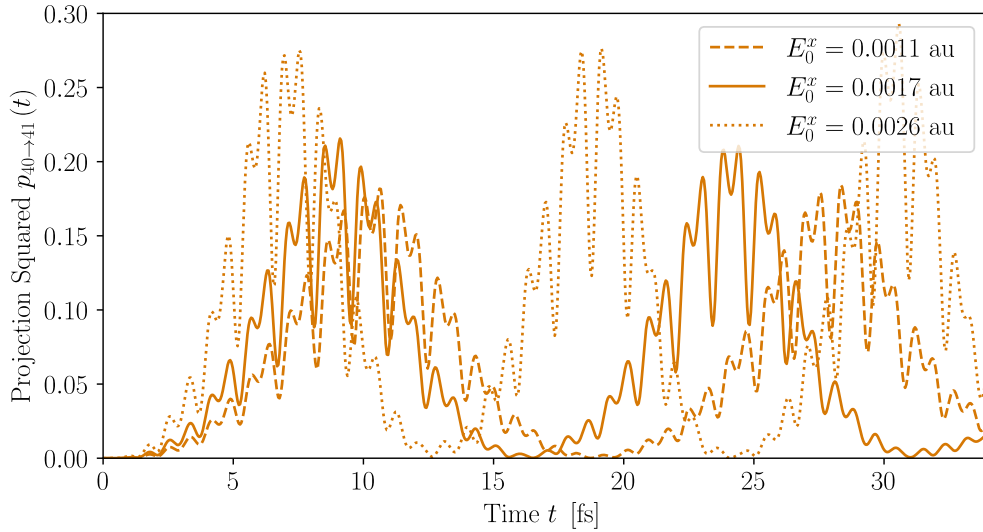


Figure 13: HOMO \rightarrow LUMO projection for three different field strengths E_0^x in otherwise identical calculations. The solid line is the calculation shown in Figure 8.

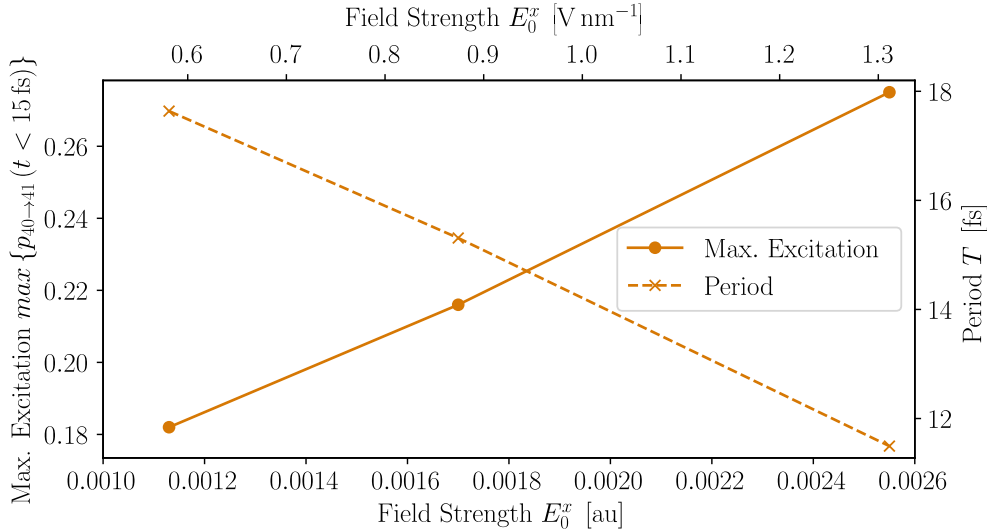


Figure 14: Period and maximum HOMO→LUMO projection as a function of field strength E_0^x from the calculations show in Figure (13). The height (solid line) is taken as the maximum value in the first peak of the main oscillation ($t \leq 15$ fs). The period (dashed line) is measured as the difference in position of the central dips between the highest two neighbouring peaks in the first peak and second peak of the main oscillation.

relationship between the period of the Rabi oscillation and the field strength used to induce it, but not necessarily a linear relationship between the maximum LUMO occupation and the field strength. Figure 14 shows that, both the period and excitation behave highly linearly with variation in the field strength. In our calculations, the maximum excitation as a function of the field strength does differ more from the linear behaviour than the period, as expected.

Charged Molecule

In her doctoral thesis, Jokar [40] describes the improvement towards in-tune Rabi oscillations gained by considering the triplet state of the a toy model, as was discussed in Chapter 2.3.2. Inspired by these findings, the goal of this section is to investigate whether a similar trend can be seen also for real systems. To this end, we repeat the simulations for a positively charged molecule and, thus, remove one electron from the highest occupied state. This leaves the HOMO with a single electron and, therefore, according to Jokar [40], should get us to a higher HOMO→LUMO transition percentage. To this end, we have repeated the linear-response calculations for the singly

positively charged molecule in both the Casida formalism (spin-polarized) and the time-propagation scheme (spin-polarized and spin-unpolarized). For spin-polarized calculations the electron has been removed from the spin-down channel.

The Casida calculation has been performed for a minimal-shaped simulation box of radius $R = 5 \text{ \AA}$ and a spacing $h = 0.12 \text{ \AA}$ with an additional 40 converged unoccupied states. In spin-polarized calculations only, the energetic order of some individual Kohn-Sham states changed due to the additional charge. Therefore, the former HOMO to LUMO transition (40→41) is now the 39→41 transition. For an overview of the change in numbering refer to Table 3. To check whether or not the charging of the molecule influences the individual Kohn-Sham states, the overlap between the neutral and charged molecule $S_{ij}^\uparrow = \langle \varphi_i^{\text{charged}} | \varphi_j^{\text{neutral}} \rangle$ has been calculated (trapezoidal integration rule) and summarized in Table 3. They show that the HOMO and LUMO from the uncharged molecule can safely be identified with the HOMO/HOMO-1 and LUMO of the charged molecule. This means that the HOMO-1 to LUMO transition still resembles the HOMO to LUMO transition for the uncharged molecule. Both time-propagation calculations,

Table 3: The change of the energetic order of the individual Kohn-Sham orbitals between the uncharged molecule and the two spin channels for the charged molecule, determined qualitatively by visual comparison. In particular, for the spin-up channel the HOMO and the HOMO-1 switch places compared to the uncharged molecule, whereas the spin-down channel remains. Orbitals that take part in the absorption peaks listed in Table 4 but not listed here remain unchanged.

Uncharged Molecule	Charged Molecule			
	Spin \uparrow Orbital number	Overlap	Spin \downarrow Orbital number	Overlap
HOMO-2 (38)	34	0.669	34	0.656
HOMO-8 (32)	35	0.162	35	0.123
HOMO-1 (39)	40	1.000	39	1.000
HOMO (40)	39	0.972	40	0.987
LUMO (41)	41	0.940	41	0.961

spin-polarized and spin-unpolarized, have been performed in the same simulation box with 10 unoccupied states to guarantee convergence. The initial kick has been a Dirac- δ with a wavevector of $k_{\text{kick}} = 0.01 \text{ \AA}^{-1}$ and the total simulation time has been $T = 70 \text{ fs}$. The results of all calculations are shown in Figure 15. From the decomposition of the Casida calculation into individual single-electron transitions, we can see that the second absorption

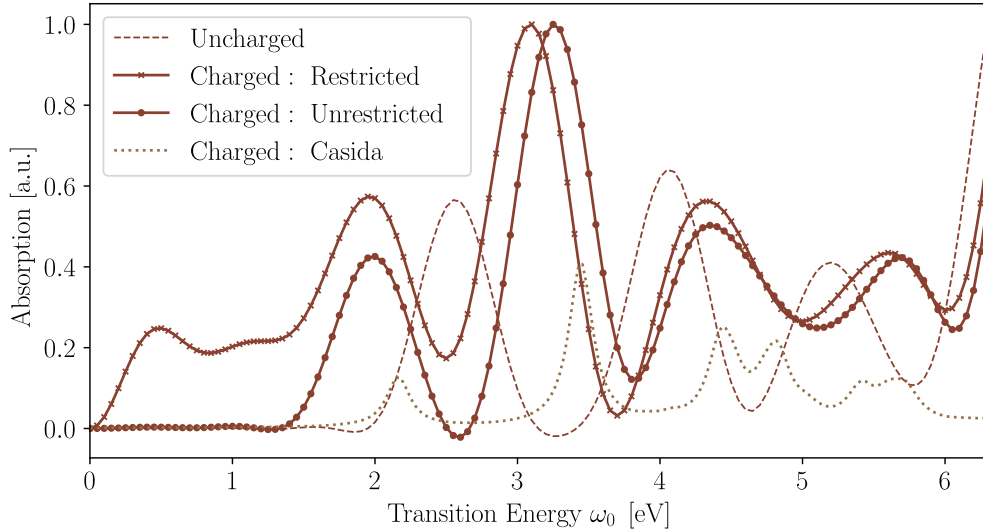


Figure 15: Time-propagation linear-response calculations for singly positively charged ANBP (solid lines) in a spin-restricted and spin-unrestricted calculation. The same calculation for the uncharged molecule (dashed line) as a comparison, as well as a spin-unrestricted Casida formalism calculation for the charged molecule. The first prominent peak is located at $\omega^{\text{res.}} = 1.95$ eV, $\omega^{\text{unres.}} = 2.00$ eV and $\omega^{\text{Casida}} = 2.18$ eV, respectively. The second dominating peak is located at $\omega^{\text{res.}} = 3.10$ eV, $\omega^{\text{unres.}} = 3.25$ eV and $\omega^{\text{Casida}} = 3.44$ eV, respectively.

peak at $\omega = 3.44$ eV has a significant contribution from the desired HOMO-1 \rightarrow LUMO (HOMO \rightarrow LUMO in the uncharged case), however, it is much less dominate as before and is even overpowered by an excitation in the spin-down channel from the HOMO-8 into HOMO. The results for a close-to-resonance driven, singly positively charged system can be seen in Figure 16 and Figure 17 for the spin-unpolarized and spin-polarized, respectively.

The spin-unpolarized calculation has been performed in a minimal-shaped simulation box with a radius of $R = 5$ Å and a spacing of $h = 0.15$ Å. The driving laser was tuned to a frequency of $\omega = 3.20$ eV with a maximum field strength of $E = 0.0017$ au and a ramp time at the start and end of $\tau = 2$ fs. The result shows a drastic improvement in terms of the amount of electrons promoted from the HOMO to LUMO state with a maximum excitation rate of $p_{40\rightarrow 41} = 0.71$. However, the results also show a complete breakdown of the Rabi oscillation after the first half cycle with a sustained high and only slowly decreasing LUMO excitation.

For the spin-polarized calculation the mesh grid density has been chosen with a spacing of $h = 0.12$ Å. The laser pulse has been tuned to a frequency of

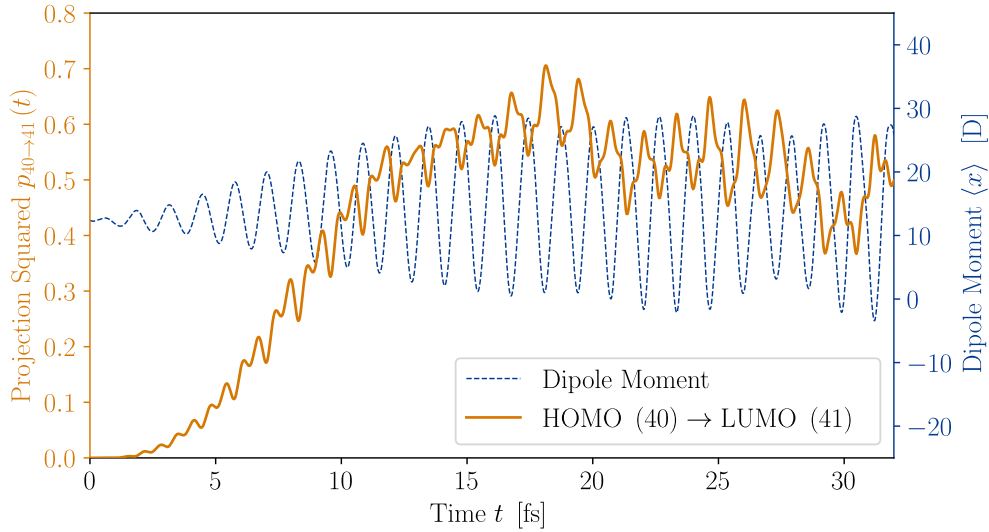


Figure 16: Time-dependent Kohn-Sham state projections $p_{40 \rightarrow 41}$ (solid orange line) and dipole moment $\langle x \rangle$ (dashed blue line) for a singly positively charged ANBP in a spin-unpolarized calculation. The laser has been tuned close to the resonance frequency with $\omega = 3.20$ eV.

$\omega = 3.25$ Å with a shallower slope of $\tau = 5$ fs. The results in Figure 17 show a very similar behaviour to the spin-unpolarized case, namely a relatively high excitation rate now from the energetically shifted HOMO-1 to the LUMO and a breakdown of the oscillatory structure with a sustained high excitation. Both observations only hold for the spin-up channel, as we see no excitation for the spin-down channel at all. This is to be expected, since the energetic order of the states for the spin-down channel, is unaffected by the removal of one electron (see Table 3). For this spin channel the excitation in question would still be the HOMO to LUMO (40→41), which is not possible since the state 40 is unoccupied in the spin-down channel.

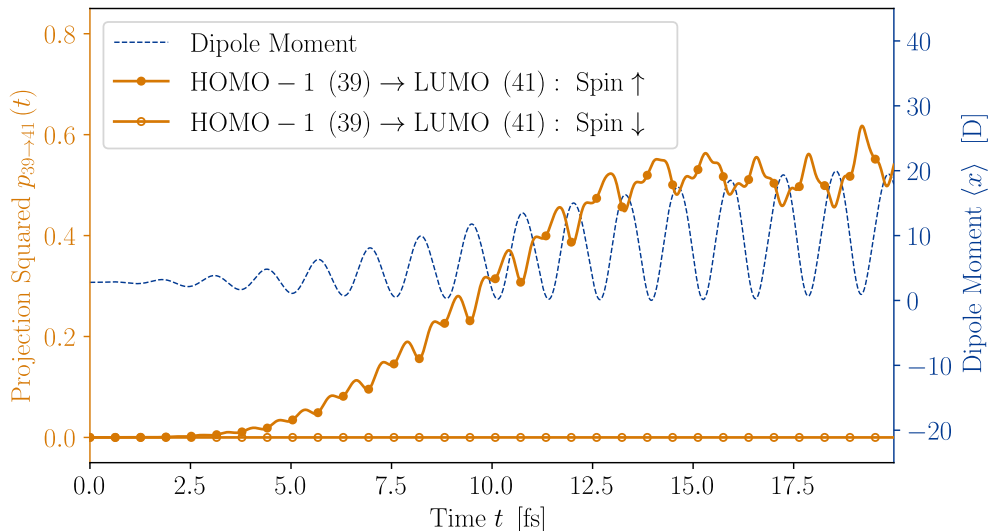


Figure 17: Time-dependent Kohn-Sham state projections $p_{39 \rightarrow 41}$ (solid orange lines; spin-up: filled markers; spin-down: unfilled markers) and dipole moment $\langle x \rangle$ (dashed blue line) for a singly positively charged ANBP in a spin-polarized calculation. The laser has been tuned close to the resonance frequency with $\omega = 3.25$ eV.

Table 4: Relative strength of the individual single-particle transitions for the first two major absorption peaks in Figure 15. Please note that, due to the net charge the energetic order of the Kohn-Sham orbital and thus the numbering changed compared to Table 2. For an overview of the reordering please see Table 3.

Transitions	Absorption Peak 1 at ≈ 2.2 eV		Absorption Peak 2 at ≈ 3.4 eV	
	Spin \uparrow [%]	Spin \downarrow [%]	Spin \uparrow [%]	Spin \downarrow [%]
29 \rightarrow 40	0.00	0.00	0.00	0.02
32 \rightarrow 40	0.00	0.00	0.00	0.42
34 \rightarrow 42	0.00	0.00	0.01	0.00
35 \rightarrow 40	0.00	0.82	0.00	0.06
35 \rightarrow 41	0.00	0.00	0.02	0.05
39 \rightarrow 41	0.16	0.00	0.36	0.00
39 \rightarrow 43	0.00	0.00	0.15	0.00

3.5 Photoemission Data

In this chapter we discuss the results of simulations of the angle-resolved photoemission process (ARPES) of ANBP with TD-DFT and the t-SURFF method. For a theoretical discussion of the method employed to record outwardly escaping photoelectrons, refer to Chapter 2.2.3.

Laser Setup

Photoelectrons are electrons excited from an occupied bound state into the continuum by a sufficiently high energetic light field. Because the angular distribution and kinetic energies of these escaping electrons carries information about the initial state of the electron, state-specific characteristic patterns emerge.

It is possible to observe these patterns even for molecular orbitals unoccupied in the groundstate in a so-called “pump-probe” setup. In this laser setup the molecule or surface is hit by two different individual laser pulses, usually separated in time. The “pump pulse” has a relatively low energy (≤ 10 eV) but high intensity. Its energy is tuned to an intra-molecular transition from an occupied state to an unoccupied state and, thus, no photoelectrons should be freed at this stage. A second, high energetic, “probe pulse” delayed in time then excites electrons from all occupied states inside the pulses energy range to the continuum. The “base” pump-probe laser setup used in this work is shown in Figure 18. For all presented pump-probe simulations, all parameters not explicitly mentioned are identical to this setup. The peak position of the \sin^2 -envelope of the probe pulse has been chosen to coincide with a peak in the HOMO→LUMO transition determined in the previous chapter.

Energy Dependent Photoemission

Figure 19 shows the total angle-integrated photoemission intensity as a function of the kinetic energy of the escaping electron for multiple pump-probe ARPES calculations. The calculations differ only in one aspect of the laser setup, derived from the setup for the calculation called “Base” shown in Figure 18, to investigate how different parameters influence the photoemission process. Common for all calculations are the spherical simulation box with a radius of $R = 25 \text{ \AA}$ and mesh grid of $h = 0.22 \text{ \AA}$, the detector surface placement at $R_d = 12.5 \text{ \AA}$ and the detector resolution of $\Delta p = 0.022 \text{ \AA}^{-1}$, $\Delta\theta = 2^\circ$ and $\Delta\phi = 2^\circ$, the complex absorbing potential boundary condition with a height of -0.75 au in the entire region outside the detector and a time step of $\Delta t = 0.0023$ fs. Additionally, all calculations have been performed within the independent particle approximation, i.e. freezing the Hartree and

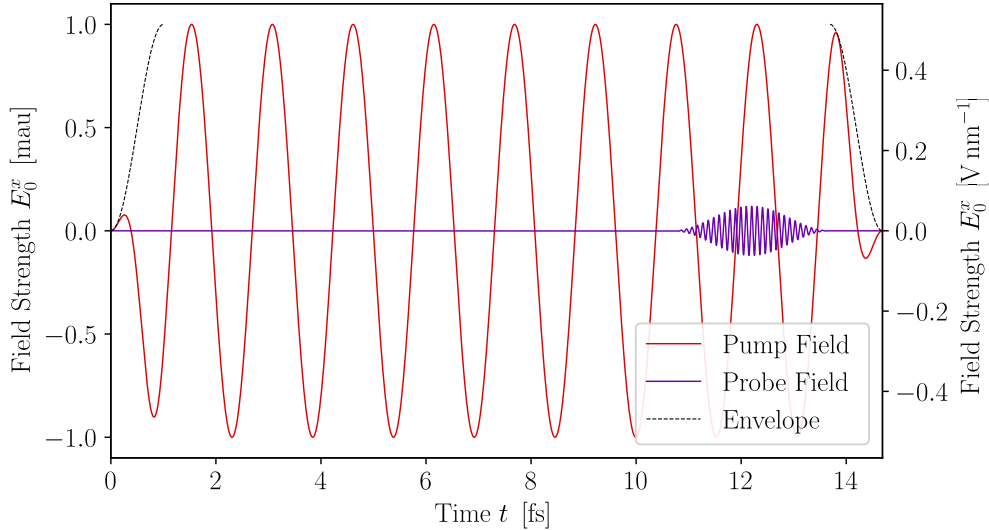


Figure 18: The “base” pump-probe laser setup used for photoemission simulations in this work. A pump pulse (solid red line) with an energy of $\omega_{\text{pu}} = 2.69 \text{ eV}$, a maximum field strength of $E_0^x = 0.001 \text{ au} \hat{=} 0.514 \text{ V nm}^{-1}$ and a sin^2 -shaped ramp (dashed black line) for the first and last $\tau = 1 \text{ fs}$. A second, delayed probe pulse (solid purple line) with an energy of $\omega_{\text{pr}} = 40 \text{ eV}$ and a maximum field strength of $E_0^x = 0.0001 \text{ au} \hat{=} 0.061 \text{ V nm}^{-1}$. The entire pulse is enveloped by one cycle of a sin^2 -function with a total pulse duration of $T = 3 \text{ fs}$. This envelope reaches its peak at $T = 12.19 \text{ fs}$. The downward slope of the envelope for the pump pulse starts at the end of the probe pulse.

exchange-correlation potential of the groundstate for all time steps.

The calculation called “Base” uses the exact laser setup described in Figure 18. Compared to that, “No Pump” has only a probe field but no pump pulse, “Large Ramp” has a swallower rise and fall of the pump field by increasing the period of the envelope function to $\tau = 2 \text{ fs}$ and “Half Pump” reduces the maximum field strength of the pump field only by a factor of two. For “Half Field” only the peak of the envelope of the probe pulse has been pushed back to $T = 18.40 \text{ fs}$, and the simulation period has been extended accordingly, to take the delayed peak in HOMO→LUMO transition caused by the weakened field into account.

Due to energy conservation, electrons escaping from a molecular state will be released with a characteristic amount of kinetic energy. This direct link between the kinetic energy of the released electron and the molecular orbital, and the simple fact that electrons can only be freed from previously occupied

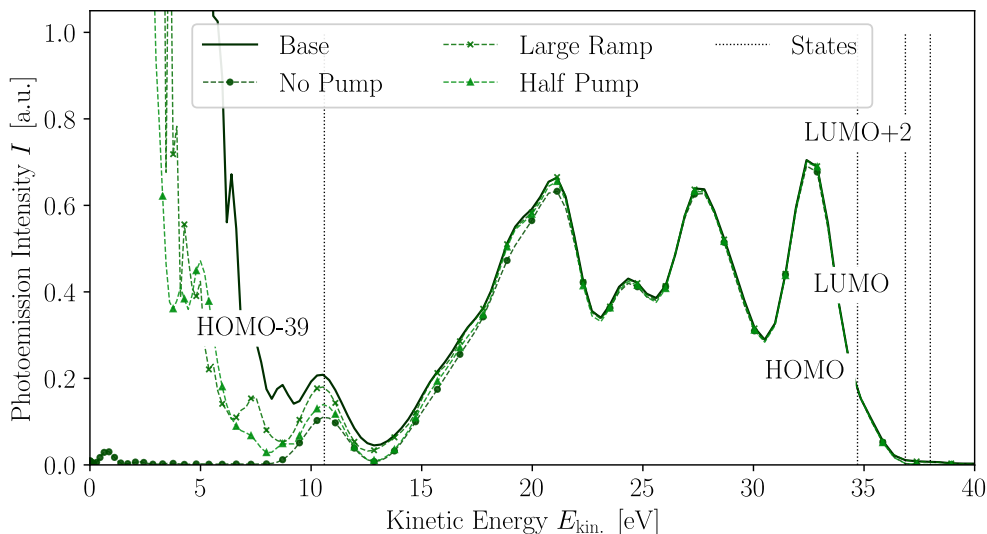


Figure 19: Total angle-integrated photoemission intensity as a function of the kinetic energy of the escaping electron. Four different calculations with slightly different laser setups derived from the base laser setup used for the calculation “Base” (solid dark green line) shown in Figure 18. For a more detailed description of the individual calculation refer to the main text. The dotted black lines show the kinetic energy of an electron escaping from the specific state labelled next to the line.

states, allows us to interpret the energy-dependent, angle-integrated photoemission intensity as density of states of the molecule.

We want distinguish between two regions in Figure 19 separated at $E_{\text{kin.}} = 10.60$ eV, the kinetic energy of the electrons escaping from lowest lying state HOMO-39 (not counting the ones covered by the pseudo-potential). The intensity of the low kinetic energy contributions are very high compared to the emissions at higher energies, however, they decrease sharply in the vicinity of the HOMO-39 emission and there is no significant contribution from them at the energy of the frontier orbitals relevant for this work. This can be seen from the “No Pump” calculation, which shows only very few low kinetic energy emissions at $E_{\text{kin.}} = 0.7$ eV. “No Field” is, however, virtually identical to the other calculations at the energy of the HOMO. This means that, first, these low kinetic energy contributions are caused by the pump field and not the probe field and second, they have no significant influence on the transition under investigation between the high lying orbitals. Any photoemission below the lowest state is either unphysical and numerical in origin or has to be the result of multi-photon processes, or possibly both. While the latter

explanation can account for the dependence on the pump field intensity, it can not account for the residual emissions seen in the “No Pump” calculation. Additionally, such high intensities of many orders of magnitude larger than the frontier orbitals seems unlikely to originate in excitations by multiple photons at once. In Appendix C the low kinetic energy contributions have been investigated for methane and the photoemission intensity recorded time-dependently. One core result this is the dependence of these low kinetic energy contributions on size of the simulation box, with larger box sizes seeing these emissions eliminated completely, at least for methane. The true nature of these emissions could not be determined conclusively.

Figure 19 also shows, that there is little to no influence of the ramp time for the pump pulse on the photoemission intensity. The strength of the pump field has, outside the low kinetic energy region, also little effect, except for a significant decrease of the emissions at the LUMO energy by 70 % that can be seen between the “Base” and “Half Pump”. This is to be expected, as a weak or no pump field results in a reduced HOMO→LUMO transition and, therefore, lower LUMO occupation.

Figure 20 shows the same calculations as Figure 19 but the photoemission intensity has been projected onto the electrons being freed from the HOMO only. This, again, shows that the low kinetic energy contributions are not

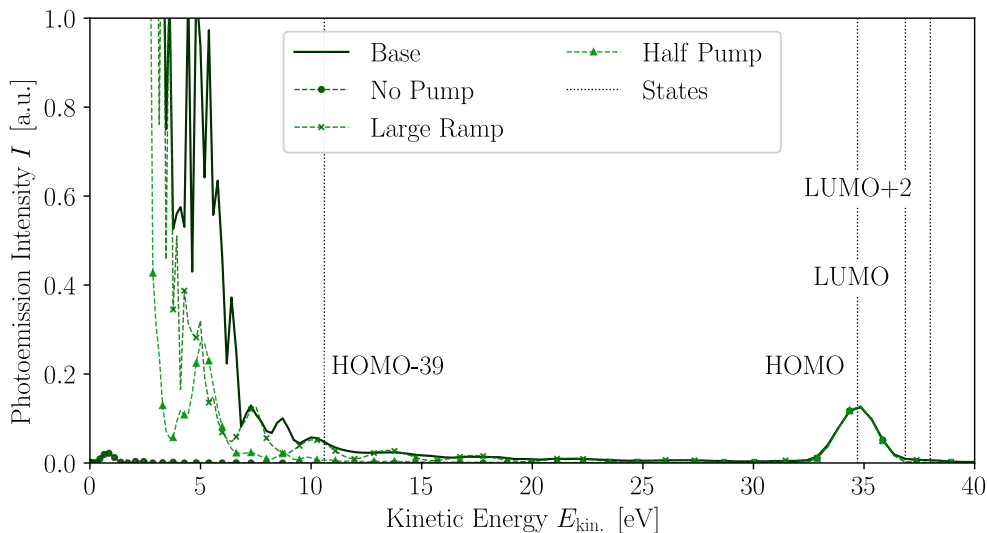


Figure 20: Identical to Figure 19 but projected onto the electrons escaping from the HOMO only.

relevant for the discussion of HOMO→LUMO transition, as there are virtually no emissions above $E_{\text{kin.}} = 25$ eV. Additionally, comparing Figure 19 and Figure 20, we observe that a majority ($\approx 71\%$) of the intensity at the HOMO energy are electrons from the HOMO. The residual intensity is bleed over from the lower lying states caused by the energy broadening. Energy broadening is a consequence of the short probe pulse duration necessary, due to relatively fast Rabi oscillation. A decrease in pump field would linearly decrease the Rabi period (see Figure 14), however, would postpone the peak LUMO occupation and, thus, increase the computational cost.

Photoemission maps (k-maps)

The photoemission intensity $\mathcal{P}(\mathbf{p})$ can be thought of as a 3D data cube in spherical coordinates with the radius $p = |\mathbf{p}|$ and the angular coordinates θ and ϕ . The upper hemisphere of a 2D slice $p = \sqrt{2 \cdot E_{\text{kin.}}}$ of this data cube at a constant kinetic energy $E_{\text{kin.}}$ can then be projected onto a Cartesian coordinate grid (k_x, k_y) by

$$k_x = \frac{p_x}{\hbar} = \frac{p}{\hbar} \cdot \sin \theta \cos \varphi$$

$$k_y = \frac{p_y}{\hbar} = \frac{p}{\hbar} \cdot \sin \theta \sin \varphi$$

The resulting flat representation of the angular distribution and intensity of the photoelectron emission at a constant kinetic energy are called “momentum maps” or “k-maps” [1]. The calculation of k-maps from ARPES simulations performed with Octopus, among many other post processing tools for Octopus calculations, have been combined within a open-source software package called “Octopost” (see Appendix D).

k-maps for “Base”, “No Pump” and “Half Pump” as well as a new calculation called “z-Pol.”, at the kinetic energy for the HOMO $E_{\text{kin.}}^{\text{HOMO}} = 34.70$ eV are displayed in Figure 21. The “z-Pol.” calculation is identical to “Base”, except for the polarisation direction of the probe pulse, which is now perpendicular to the plane of the molecule (the z -direction) instead of along the long axis of the molecule (x -direction). The k-maps for “Base”, “No Pump” and “Half Pump” at the HOMO energy are very similar in both features, positions of these features and relative intensities. The brightest feature centred at $(k_x = 1.642 \text{ \AA}^{-1}, k_y = 0.000 \text{ \AA}^{-1})$ increases slightly in intensity from “Base” ($\mathcal{P} = 2.819$) to “Half Pump” ($\mathcal{P} = 2.893$) to “No Pump” ($\mathcal{P} = 2.921$). This can be explained by a decrease in HOMO→LUMO transition and subsequent increase in HOMO occupation due to the weaker or non-existent pump field. The (k_x, k_y) position of this feature is completely unaffected. Further notice-

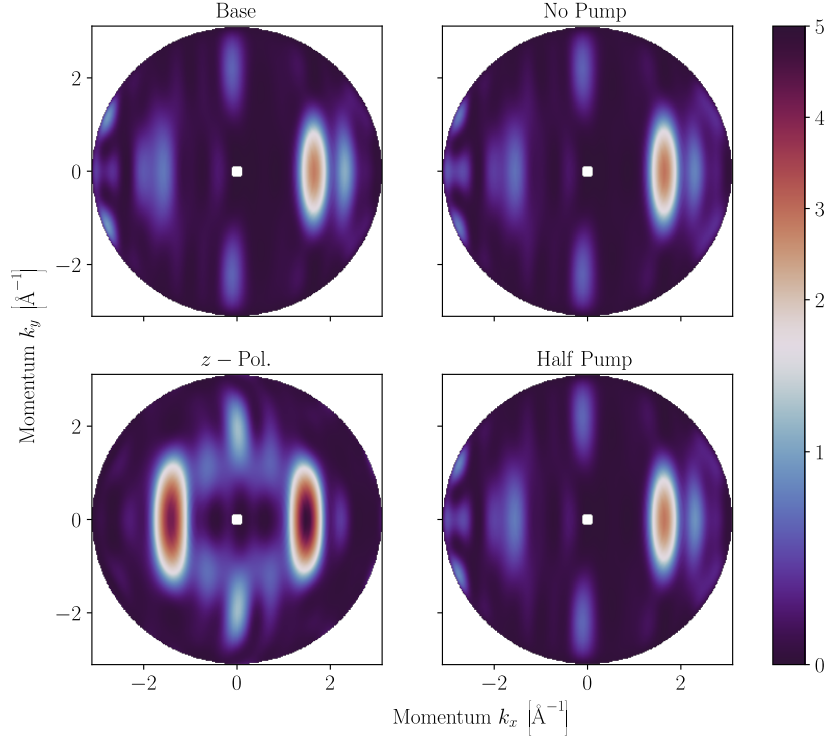


Figure 21: k-maps at a kinetic energy $E_{\text{kin}}^{\text{HOMO}} = 34.70 \text{ eV}$ corresponding to the HOMO state. Note that in order to increase the contrast in darker areas the colour map is split into two separate linear regions, from 0 to 1.5 and from 1.5 to 5. This highlights low intensity areas compared high intensity ones.

able is the asymmetry present along the k_x direction, due to the asymmetry of the initial state molecular orbital HOMO. The intensity at $k_x \rightarrow -k_x$ is around one fourth of the maximum value and is not completely aligned with the bright spot in this area at $(k_x = -1.556 \text{ \AA}^{-1}, k_y = 0.000 \text{ \AA}^{-1})$. There is no asymmetry along the k_y direction. The “z-Pol.” has only some similarities with the other calculations. There also exists an asymmetry between the brightest feature at $(k_x = 1.468 \text{ \AA}^{-1}, k_y = 0.000 \text{ \AA}^{-1})$ and $(k_x = -1.468 \text{ \AA}^{-1}, k_y = 0.000 \text{ \AA}^{-1})$, but to much smaller degree (only 15%). An additional asymmetry can be seen in the feature at $k_x = 0.000 \text{ \AA}^{-1}$, bending slightly towards negative values of k_x . While similar features at this position can be found in the other three calculations, they do not show any bending. The maximum photoemission intensity is also larger with a maximum values of $\mathcal{P} = 4.879$ compared to the maximum of $\mathcal{P} = 2.921$ in “No Pump”.

Several other features like the pronounced double peak structure around the bright spots discussed before and the feature at around $k_x = -3 \text{ \AA}^{-1}$ are missing or are significantly weaker in “ z -Pol.”.

Figure 22 shows the same four calculations at the kinetic energy corresponding to the LUMO at $E_{\text{kin.}}^{\text{LUMO}} = 36.87 \text{ eV}$.

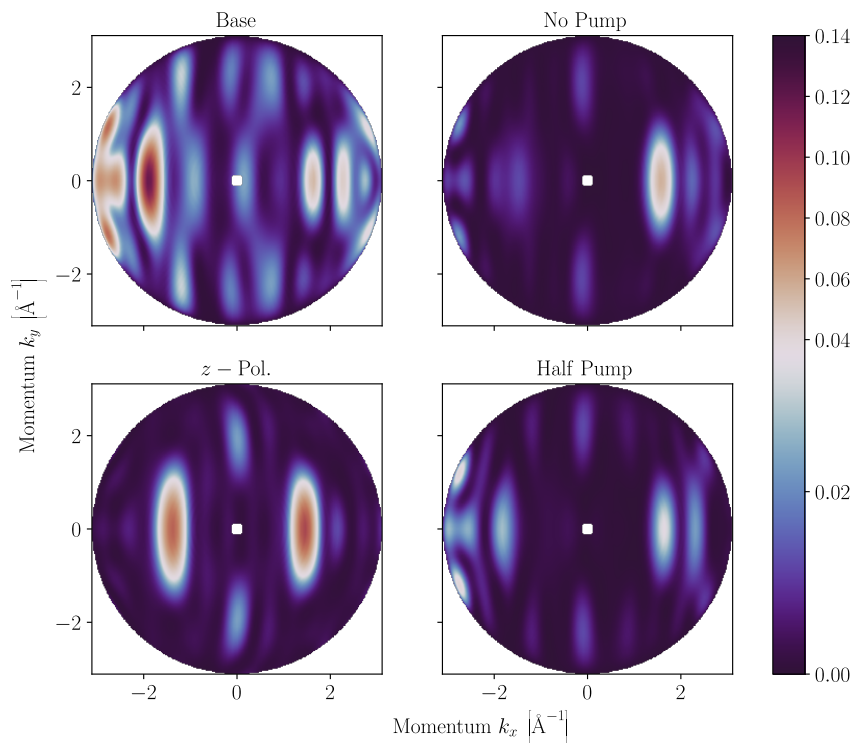


Figure 22: k -maps at a kinetic energy $E_{\text{kin.}}^{\text{LUMO}} = 36.87 \text{ eV}$ corresponding to the LUMO state. Note that in order to increase the contrast in darker areas the colour map is split into two separate linear regions, from 0 to 0.05 and from 0.05 to 0.14. This highlights low intensity areas compared high intensity ones.

All four calculations show a large decrease in photoemission intensity for the LUMO energy compared to the HOMO energy (less than 1/30), which is to be expected as none of these calculations, as seen in the previous chapter, reaches a full LUMO occupation. For the calculation “No Pump”, the k -map at the LUMO energy looks more or less identical to the one at the HOMO energy, barring the reduced intensity. This is to be expected, as the probe pulse in the “No Pump” calculation meets the groundstate of the molecule

unexcited by any previous laser pulse. The only photoemission possible in this case is, therefore, photoelectrons released from the occupied orbitals HOMO and below. With the HOMO being the closest to the LUMO energy, we see only the bleed over from the HOMO at this energy.

Due to this leakage, we generally expect to see a mixture between HOMO and LUMO emissions and going from “No Pump” to “Half Pump” to “Base”, we expect a gradually increase in intensity for features related to the LUMO. Indeed, there is an increase in intensity in features for negative k_x , with even an inversion of the asymmetry in “Base”. This inversion of asymmetry can be explained by the inversion of asymmetry between the HOMO and LUMO orbital. However, many of the features that increase in intensity from “Half Pump” to “Base”, and could, therefore, possibly be attributed to the LUMO, are also present in the “No Pump” k-map and the k-maps at the HOMO energy, although to a lesser extent. This means that, either they are at least partly due to overlap with other orbitals, also inherent to the HOMO or the probe pulse causes some LUMO occupation by excitation from an occupied state.

Additionally, “Base” shows an relatively pronounced emission pattern outside at $-1.5 \text{ \AA}^{-1} < k_x < 1.5 \text{ \AA}^{-1}$ only hinted at in the “Half Pump” calculation. The origin of these pattern could be further, weaker emissions from the LUMO or emissions of other orbitals.

“z-Pol.” shows a very similar pattern at the LUMO energy as it does for the HOMO energy, suggesting the importance of the polarization direction on the photoemission pattern. The bending of the straight emission lines at $k_x = 0 \text{ \AA}^{-1}$ are still present, and not replicated by any other calculation. The asymmetry got weaker, but did not invert unlike in “Base”, the calculation with an identically strong pump pulse. However, minor features in the regions $-1 \text{ \AA}^{-1} < k_x < -0.2 \text{ \AA}^{-1}$ and $0.2 \text{ \AA}^{-1} < k_x < 1 \text{ \AA}^{-1}$ did reduce in intensity relative to the main features discussed before. One possible explanation could be, that these are bleed over emissions from lower lying orbitals, decreasing in intensity as one moves further away towards higher kinetic energies.

One issue in interpreting k-maps this way is the fact, that we do not have a pure LUMO or a pure HOMO map to compare it to in order to unequivocally identify features associated with either. One way to mitigate this problem, is to compare k-maps from TD-DFT with the results of other methods to identify common patterns. In particular, we want to compare the results shown in Figure 21 and Figure 22 to the so called “plane-wave final state approach” (PW) [1]. Figure 23 shows the k-maps at the HOMO and LUMO energy

from the “Base” calculation on the top row compared to the corresponding k-maps for the PW on the bottom row. The k-maps for PW have been generated using the groundstate DFT calculation from an online database (ID 473) for organic molecules [64] and the software kMap.py [65].

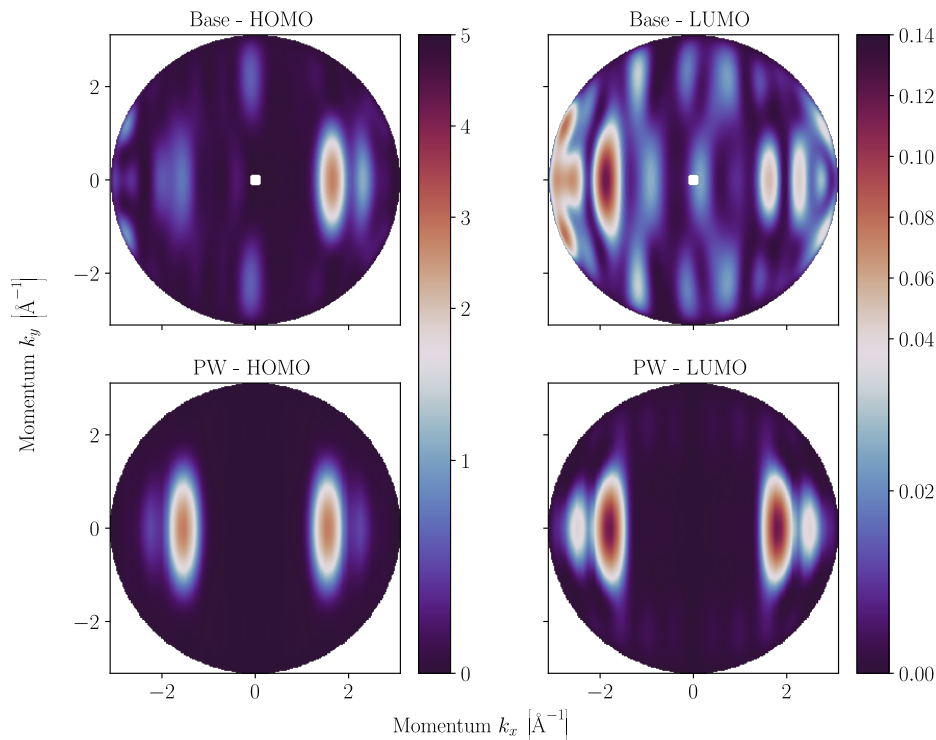


Figure 23: Comparison of k-maps at the energy for the HOMO (left column) and LUMO (right column) from the TD-DFT calculation (top row) done in this work with the plane-wave final state approach (PW; bottom row). The k-maps for the PW have been generated from Kohn-Sham orbitals from an online database [64] (ID 473) and the software kMap.py [65].

In this comparison, we first note the absence of any asymmetry along the k_x direction for the PW. In fact, for a molecule symmetric under $(x, y, z) \rightarrow (x, -y, -z)$ inversion, k-maps generated with PW will always have a $k_x \rightarrow -k_x$ symmetry. ANBP does have this symmetry and, therefore, we cannot expect an asymmetry in PW k-maps. Additionally, we note the absence of any feature at $k_x = 0 \text{ \AA}^{-1}$ for PW k-maps. In the PW the polarisation enters via a factor of the form $|\mathbf{A} \cdot \mathbf{k}|$, where \mathbf{A} is the vector potential of the electric field. Thus, any intensity in a momentum direction perpendicular to the

polarisation of the probe field will be suppressed by this factor. For the x -polarisation used here this means that, we cannot expect any emission along the $k_x = 0 \text{ \AA}^{-1}$ line. Keeping these two shortcomings of the PW in mind, we observe an overall similarity between results of the computationally and theoretically much more involved TD-DFT calculation and the PW for the HOMO. The PW does reproduce the shape and position of the bright spot at $(k_x = 1.6 \text{ \AA}^{-1}, k_y = 0.000 \text{ \AA}^{-1})$ and its double peak structure towards the outer edge. It does not, however, capture the full feature at $k_x = -3 \text{ \AA}^{-1}$, which is visible for the HOMO and pronounced for the LUMO, nor does it show any finer structure in the central area that is hinted at in the HOMO. For the latter, this could be an indication that they are, in fact, leakage effects from other orbitals not possible in PW. The former, which we hoped to identify as part of the LUMO emission due to its increase in intensity with stronger pump fields, is only partly visible in the LUMO k-map in the PW. We can, therefore, not be certain about the identification of this feature as part of the LUMO emission pattern. Also, noticeable absent is the pronounced, fine structure observed in the TD-DFT calculation for “Base”, hinting, again, at the possibility of leakage effects from other orbitals.

Charged Molecule

As a last step, we present the results of the photoemission simulation for the singly positively charged molecule (“SE”). The computational details of the simulation are identical to “Base”, with the exception of the removal of one electron from HOMO and the consequences thereof, namely the change in energy for the pump pulse to $\omega_{\text{pu}} = 3.2 \text{ eV}$ and the peak of the envelope of the probe pulse at $T = 18.13 \text{ fs}$, to capture the peak HOMO→LUMO excitation. All calculation in this chapter have been done in a spin-unpolarized scheme to reduce the computational cost. Figure 24 shows the total angle-integrated photoemission intensity as a function of the kinetic energy of the released photoelectron (“SE”) in comparison to the uncharged molecule (“Base”). After a shift of around $\Delta E = 3.5 \text{ eV}$ into account, the photoemission spectrum for the charged and uncharged molecule are relatively similar in peak structure and shape. A stark contrast, however, is the much reduced intensity of the low kinetic energy contribution in the charged case. Figure 25 compares the k-map for the charged (bottom row) and uncharged (top row) molecule at the respective energies for the HOMO (left column) and LUMO (right column). Even though the overall photoemission intensity for LUMO went down, not up as one would expect from a higher LUMO occupation, the k-map for the charged molecule does indeed resemble the one from the uncharged molecule. Furthermore, it seems to highlight feature we previously

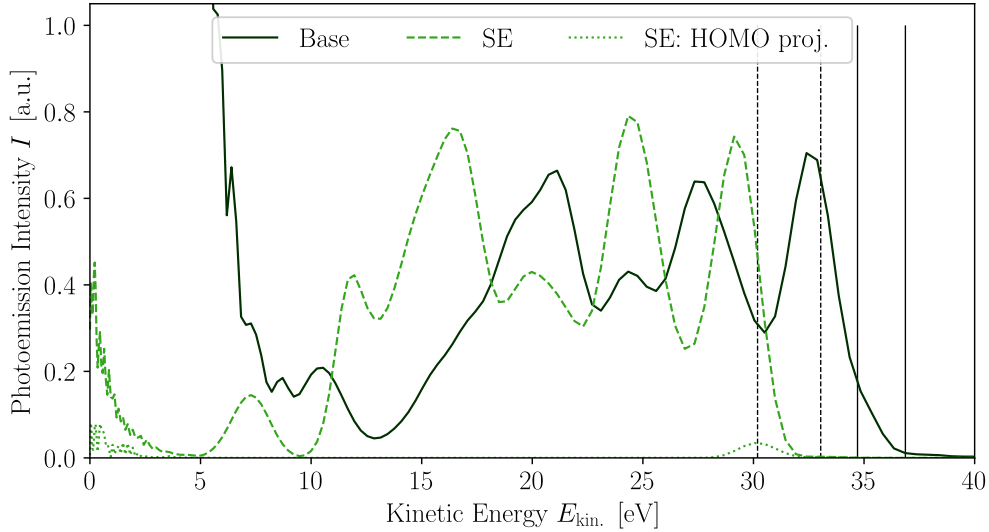


Figure 24: Total angle-integrated photoemission intensity as a function of the kinetic energy of the photoelectron for the singly positively charged ANBP molecule (dashed light green line) with the photoemission spectrum of the “Base” calculation (solid dark green line) as comparison. For the charged calculation the photoemission intensity projected onto the electrons freed from the HOMO only is also plotted (dotted light green line). Black lines show the position of emission from the HOMO and LUMO for the charged molecule (dashed) and uncharged molecule (solid), respectively.

(Figure 22) already tried to identify with the LUMO, namely the asymmetry in favour of negative values of k_x and the edge feature at that $k_x = -3 \text{ \AA}^{-1}$. The finer structure that is so pronounced in “Base” compared to, for example, “Half Pump” is also barely detectable. Overall, the clear prominence of the former in “SE”, that comes with relatively a high LUMO occupation, gives us confidence in identifying the them as a LUMO-related pattern, whereas, the verdict on the finer structure is still less clear. Compared to that, the k-map for charged case at the energy of the HOMO does not show any commonality with the uncharged case. This result is surprising, considering the relatively good agreement of the k-map for the LUMO. However, comparing the k-map at HOMO energy for “Base” with the k-map from “SE” at the kinetic energy $E_{\text{kin.}} = 31.77$ (see Figure 26), we can recognize distinct HOMO related patterns. We want to emphasize that, the energy for the k-map of the “SE” calculation in Figure 26 does not correspond to the binding energy of any state at seems to be in between the energy $E_{\text{kin.}} = 30.18 \text{ eV}$ for the HOMO and the energy $E_{\text{kin.}} = 33.04 \text{ eV}$ for the LUMO. Interpretation as the

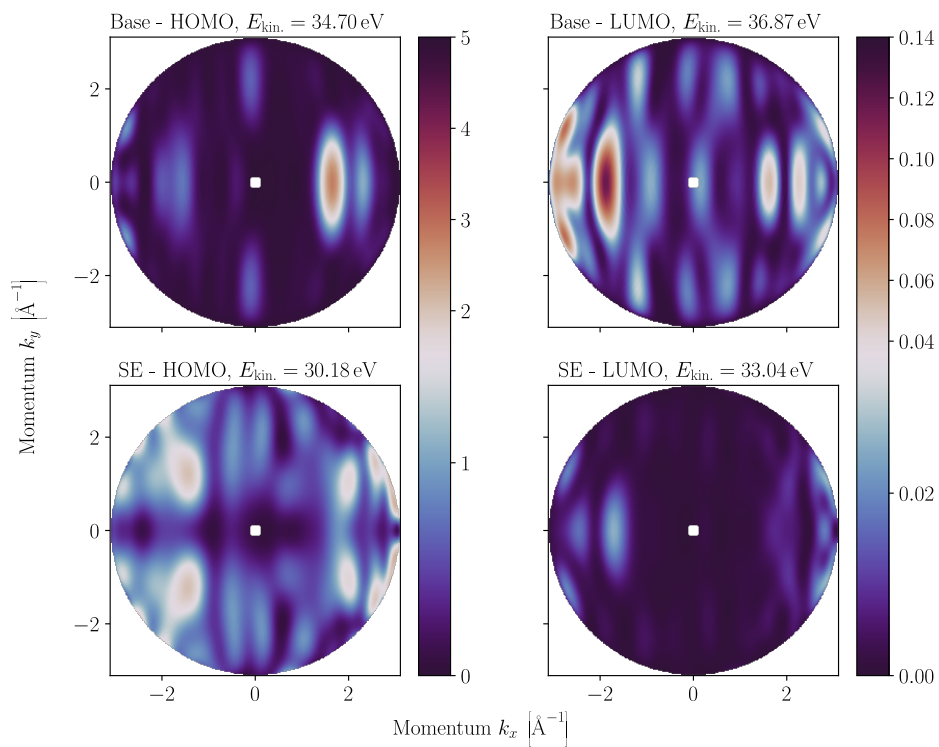


Figure 25: Comparison of k-maps between “Base” (top row) and “SE” (bottom row) at the respective energies for the HOMO (left column) and LUMO (right column).

k-map for the HOMO is not easily possible. A possible reason for this shift in energy could be that, this charged open-shell system has been calculated in a spin-restricted scheme.

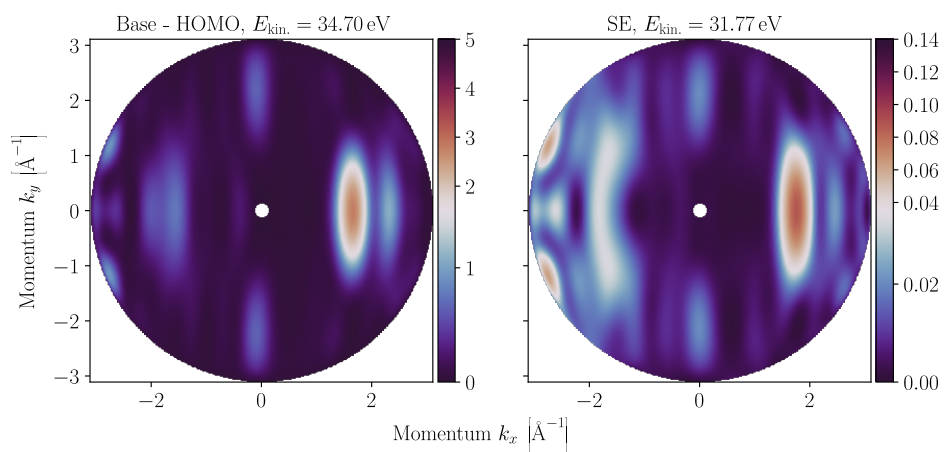


Figure 26: Comparison between the k-map at the kinetic energy associated with the HOMO from “Base” with a k-map from “SE” at a particular kinetic energy ($E_{\text{kin.}} = 31.77 \text{ eV}$) between the HOMO and LUMO.

3.6 Ehrenfest Dynamics

As a last step in this work, we investigate the influence of the nuclear motion on the Rabi physics observed with TD-DFT. Outside geometry relaxation procedures, density functional theory calculations are, in general, within the clamped nuclei approximation, i.e. freezing the cores of the individual atoms in place. However, after excitation by an external electric field, the electronic structure of the system is, in general, forced out of the groundstate equilibrium. This, in turn, would induce nuclear motion, if not for the fact that the nuclei are artificially fixed in space. This motion is, due to the mass difference between electrons and nuclei, in general, much slower.

Using the Ehrenfest scheme described in Chapter 2.2.4, we can loosen this restriction and allow vibrational modes in the atomic structure, which, in turn, also influences the electronic structure and, therefore, the Rabi physics observed. In particular, it will change the energy levels of the individual orbitals. The influence of this on the Rabi oscillation is hard to predict, but one might expect a further detunement due to a possible relative shift of energy levels and subsequent change in transition energy. Another possible outcome is the breakdown of the Rabi oscillation all together as a result of decoherence.

Figure 27 shows the HOMO→LUMO projection squared and the $C_1 - C_{1'}$ bond length between the carbon atoms connecting the two aromatic rings.

This calculation was performed in a “minimal”-shaped box with radius of $R = 5 \text{ \AA}$ and a spacing of $h = 0.10 \text{ \AA}$, a time step of $\Delta t = 0.0005 \text{ fs}$ and Ehrenfest dynamics enabled. The external field consisted of a pump probe only, tuned to the transition dominated by the HOMO→LUMO transition at $\omega = 2.70 \text{ eV}$ and with a maximum electric field strength of $E_0^x = 0.0017 \text{ au} \hat{=} 0.872 \text{ V nm}^{-1}$. The envelope of the laser pulse was trapezoidal with a ramp time of $\tau = 5 \text{ fs}$ at the beginning and end.

The bond length changes depicted in Figure 27 are not characteristic for an excitation of a single dominant mode for the nuclear motion, but instead a mixture of them resulting in a complicated behaviour in time. Experimental results yield a vibrational frequency of $\nu = 1608 \text{ cm}^{-1} \hat{=} 20.74 \text{ fs}$ for the bridging inter-ring $C_1C_{1'}$ bond stretch of biphenyl (without the functional groups) [66]. This roughly coincides with the distance between the first and second maxima indicated in the figure. As for the projection, no influence on the Rabi physics can be observed for the first cycle. This likely due to the relatively slow motion of the nuclei not yet showing any influence on the electronic structure. After the first cycle, the next cycle is shortened by $\Delta T = 3.1 \text{ fs}$. However, this shift stays constant for the third cycle and

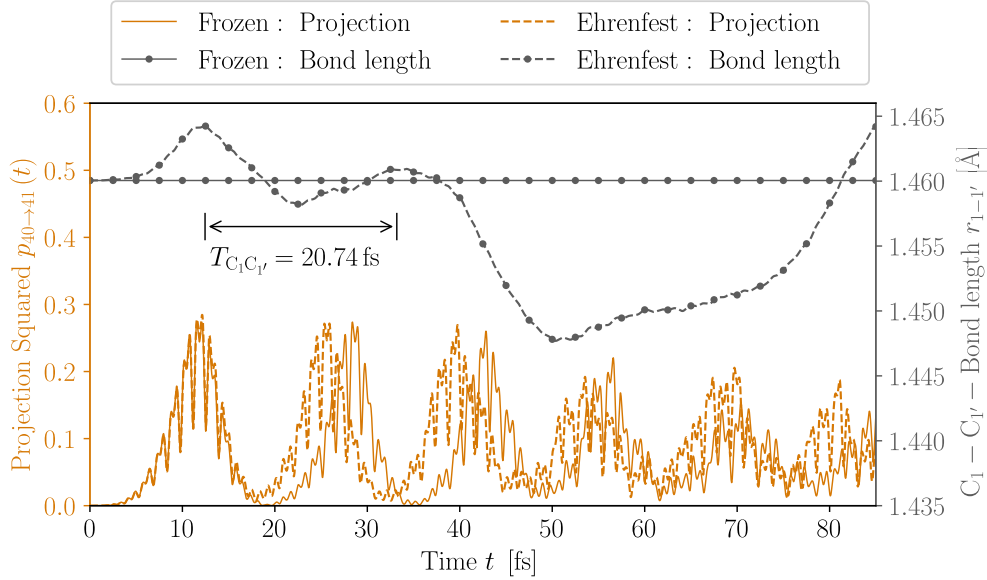


Figure 27: Comparison between a clamped nuclei (“Frozen”) calculation and one with nuclear motion allowed (“Ehrenfest”). The inter-ring C-C bond length $r_{1-1'}$ between the phenyl rings (line with markers) and the HOMO→LUMO projection squared (line without markers) are displayed. The experimentally determined period $T_{C_1C_{1'}}$ for the bond stretch in biphenyl are shown as well [66].

there is no further shortening, meaning that only the second cycle is shortened. Furthermore, we do not see any significant change in HOMO→LUMO transition between the frozen nuclei calculation and the Ehrenfest dynamics. Starting from cycle three, the oscillation seems to be breaking down for both calculations. Again, there is no significant change by the introduction of nuclear motion.

4 Conclusion and Future Prospects

The research goal for this thesis, outlined in Chapter 1, was the theoretical description of the photoemission process of 4-Amino-4'-nitrobiphenyl using time-dependent functional theory. The motivation thereof, is a sub-femtosecond pump-probe photoemission experiment currently in the planning stage, realizing the next step in our understanding of matter-light interaction: orbital cinematography. This goal was achieved insofar that, momentum maps for both the groundstate HOMO and even the via excitation partly occupied LUMO have been produced. Furthermore, issues of using TD-DFT as the theoretical framework for the description of ARPES and possible remedies have been investigated.

In this chapter, we recall the core results of this thesis and indicate potential future directions for follow-up research projects.

After a fairly routine geometry optimization of the atomic structure of the molecule in DFT, time-dependent density functional theory in three different schemes has been used to calculate the absorption spectrum of the system. This has revealed the resonant energies for a potential pump pulse, driving the exact transition we are interested in between the HOMO and LUMO. Although issues with the convergence with regards to the grid spacing occurred (Figure 6), the transition energy has been determined successfully and with good agreement between the individual schemes used.

A main effort was to investigate to which extent the Rabi physics for a HOMO-LUMO transition can be simulated within the framework of TD-DFT. However, this turned out to be difficult as adiabatic xc-functionals used in time-dependent density functional struggle with this exact task. Already described in the literature for toy models, this has also been demonstrated for a real system. Experiments, in general, do not achieve a full population inversion between the HOMO and LUMO either. However, this could nonetheless pose an issue for future research projects, as there is no pure momentum map for the LUMO calculated in the framework of TD-DFT available to compare the results to. This makes identifying or interpreting individual features more difficult. Nevertheless, features in the momentum maps were identified, which we associate with the LUMO to a high degree of confidence. This was possible by removing an electron from the HOMO, following the findings of Jokar [40].

The influence of the atomic movement on the Rabi physics has been investigated by releasing the otherwise clamped nuclei. It has been determined to have little influence on the Rabi oscillation, only slightly decreasing the period.

Last, we outline potential goals for future research projects building on what has been done here.

Without any experimental data it is difficult to conclude the exact nature of the mismatch between the idealized two-level Rabi physics and the less-than-resonant behaviour observed for the real system using TD-DFT. One possible direction would be, to try to further improve the maximum LUMO occupation reached during a single Rabi cycle. This would allow for less ambiguous momentum maps of the LUMO and subsequently an easier interpretation of future experimental data. Possible ways to do that are, potentially costly, spin-polarized calculations, changing the system in question to one with an inherently odd number of electrons, higher kinetic energy resolutions around the Fermi level for the ARPES calculations or a fine tuning of the pump laser.

The probe pulse used in this work, although already quite short, is still too large to provide the time-resolution needed in orbital cinematography. Going to shorter pulses has the consequence of reducing the energy-resolution possible. Thus, a potential better way would be to try to slow the Rabi oscillation instead. At an increased computational cost, this would possible allow for a probing of the entire oscillation.

A Example usage: Octopus

This appendix shows the input file used to calculate the momentum maps for “Base” displayed in Figure 21 and Figure 22 and the relaxed geometry `relax.xyz` (see Chapter 3.2) for ANBP referred to in the Octopus input file. It serves as an example on how the software Octopus can be used to simulate the photoemission process in the manner described throughout this thesis. For details to the individual parameters, refer to Chapter 3.5.

inp

```
# Calculation #####
CalculationMode = td
ExperimentalFeatures = yes
FromScratch = yes
TDFreezeHXC = yes # independent particle approximation
PseudopotentialSet = hgh_lda
#####

# Parallelisation #####
ParStates = 40
ParDomains = 6
#####

# Photon Field #####
c_light = 137.036 # atomic units

omega_pump = 0.098860981223 # a.u. = 2.69 eV
omega_probe = 40*eV

# Laser intensity
I_probe = 5e8 # W/cm^2

# Electric field strength
E_pump = 0.001 # a.u.
E_probe = sqrt(I_probe / 3.51E16)

# Vector potential amplitude
A_pump = E_pump * c_light / omega_pump
A_probe = E_probe * c_light / omega_probe
```

```

# Laser times
T_probe = 3*fs # total probe time
tau1 = 1*fs # ramp time for the pump pulse
peak_time = 12.19*fs # peak LUMO occupation
start_probe = peak_time - T_probe/2 # begin of probe pulse
end_probe = peak_time + T_probe/2 # end of probe pulse
tau0 = end_probe - tau1 # max. pump intensity duration

%TDEexternalFields
vector_potential | 1 | 0 | 0 | omega_pump | "pump"
vector_potential | 1 | 0 | 0 | omega_probe | "probe"
%

%TDFunctions
"pump" | tdf_from_expr | "A_pump * (
    sin((t/tau1)*pi/2)^2*step(tau1-t)
    + step(t-tau1)*step(end_probe-t)
    + sin(((end_probe+tau1-t)/tau1)*pi/2)^2
    * step(t-end_probe)
    )"
"probe" | tdf_from_expr | "A_probe *
    sin((t-start_probe)*pi/T_probe)^2
    * step(end_probe-t)
    * step(t-start_probe)"
%
#####

# Molecule #####
XYZCoordinates = 'relax_centered.xyz'
#####

# Simulation Box #####
BoxShape = sphere
Radius = 25*angstrom
Spacing = 0.22*angstrom
#####

# Boundary Conditions #####
AbsorbingBoundaries = cap
ABCHeight = -0.75

```

```

%ABShape
  Radius / 2 | Radius
%
#####

# Time Propagation #####
TDPropagator = aetrs
TDTimeStep = 0.0023*fs # 6387 steps
TDPropagationTime = end_probe + tau1 # 14.69 fs
#####

# Photoelectron Spectrum #####
PhotoElectronSpectrum = pes_flux
PES_Flux_Radius = Radius / 2
N_k = 150
%PES_Flux_ThetaK
  0 | pi/2 | 45
%
%PES_Flux_PhiK
  0 | 2*pi | 180
%
PES_Flux_Kmax = sqrt(2*omega_probe)
PES_Flux_Kmin = 0
PES_Flux_DeltaK = (PES_Flux_Kmax - PES_Flux_Kmin) / N_k
PES_Flux_Parallelization = pf_time + pf_surface
#####

# Output #####
PhotoelectronSpectrumOutput = velocity_map
PES_Flux_RuntimeOutput = yes
OutputFormat = vtk
RestartWriteInterval = 500
OutputInterval = 500
#####

```

relax.xyz

26

C	-2.839273022700368188	-1.204165846862006006
O	0.000000000000000000	
H	-3.417560626105544230	-2.131646652826162835
O	0.000000000000000000	
C	-2.839273022700368188	1.204165846861986466
O	0.000000000000000000	
H	-3.417560626105544230	2.131646652826145072
O	0.000000000000000000	
C	-1.462828568088646364	-1.195246700438850951
O	0.000000000000000000	
H	-0.939477031434176269	-2.153967751726307611
O	0.000000000000000000	
C	-1.462828568088646364	1.195246700438886478
O	0.000000000000000000	
H	-0.939477031434176269	2.153967751726291624
O	0.000000000000000000	
C	1.469190895589608914	-1.187289996631999855
O	0.000000000000000000	
H	0.953654664515802608	-2.151327105893619418
O	0.000000000000000000	
C	1.469190895589608914	1.187289996632031830
O	0.000000000000000000	
H	0.953654664515802608	2.151327105893621194
O	0.000000000000000000	
C	2.844617696953420705	-1.195952586181872945
O	0.000000000000000000	
H	3.383228503074345639	-2.149475061696954015
O	0.000000000000000000	
C	2.844617696953420705	1.195952586181896038
O	0.000000000000000000	
H	3.383228503074345639	2.149475061696968226
O	0.000000000000000000	
C	-3.519905129229172758	0.000000000000000000
O	0.000000000000000000	
C	-0.730024256336132993	0.000000000000000000
O	0.000000000000000000	

C	0.730024256336129440	0.000000000000000000
	0.000000000000000000	
C	3.569398338866644593	0.000000000000000000
	0.000000000000000000	
N	-4.965194823483431108	0.000000000000000000
	0.000000000000000000	
O	-5.534207248425362380	-1.083227446386295867
	0.000000000000000000	
O	-5.534207248425362380	1.083227446386288761
	0.000000000000000000	
N	4.925513190742847769	0.000000000000000000
	0.000000000000000000	
H	5.445810154378179391	0.869518483806725584
	0.000000000000000000	
H	5.445810154378179391	-0.869518483806716702
	0.000000000000000000	

B Example usage: GPAW

This appendix shows the input file used to relax the geometry of ANBP (see Chapter 3.2) with the software GPAW from the starting guess `force_field.xyz`, obtained via force field calculation.

```
relax.py
```

```
from gpaw import GPAW
from ase.io import write, read
from ase.optimize import QuasiNewton

# Parameter
vacuum = 14 # distance between molecule and box in A
fmax = 0.02 # maximal atomic force in eV/A
spacing = 0.16 # meshgrid spacing in A

molecule = read('force_field.xyz', format='xyz')
calc = GPAW(mode='fd', xc='LDA', txt='relax.out',
            h=spacing, parallel={'sl_auto': True,
                                'use_elpa': False})

# Structure Optimization
molecule.set_calculator(calc)
molecule.center(vacuum=vacuum)
molecule.get_potential_energy()

relax = QuasiNewton(molecule, logfile='qn.log',
                   trajectory='relax.traj')
relax.run(fmax=fmax)

molecule.get_potential_energy()

calc.write('relax.gpw', mode='all')
write('relax.xyz', molecule, format='xyz')
```

force_field.xyz

26

C	-2.15579	-1.20626	0.00000
H	-2.67624	-2.16204	0.00000
C	-2.15579	1.20626	0.00000
H	-2.67624	2.16204	0.00000
C	-0.75214	-1.19611	0.00000
H	-0.26715	-2.16832	0.00000
C	-0.75214	1.19611	0.00000
H	-0.26715	2.16832	0.00000
C	2.25667	-1.18938	0.00000
H	1.78220	-2.16536	0.00000
C	2.25667	1.18938	0.00000
H	1.78220	2.16536	0.00000
C	3.66190	-1.18984	0.00000
H	4.18570	-2.14221	0.00000
C	3.66190	1.18984	0.00000
H	4.18570	2.14221	0.00000
C	-2.85368	0.00000	0.00000
C	0.00000	0.00000	0.00000
C	1.50140	0.00000	0.00000
C	4.37820	0.00000	0.00000
N	-4.32069	0.00000	0.00000
O	-4.89746	-1.09708	0.00000
O	-4.89746	1.09708	0.00000
N	5.75762	0.00000	0.00000
H	6.27407	0.86827	0.00000
H	6.27407	-0.86827	0.00000

C Low Kinetic Energy Emissions

For the energy-dependent photoemission (e.g. Figure 19) calculated in Chapter 2.2.3 we noted a large contribution to the photoemission intensity in the low kinetic energy region of the spectrum, which we deemed as either as unphysical or originating from multi-photon processes. We also observed that, the presence of these emissions being dependent the pump field, rather than on the probe field.

Even though we concluded that, these emissions have no relevant influence on the photoemission of the frontier orbitals of interest for us, in this chapter we want to present further data on these low kinetic energy emissions obtained. To this end, we chose methane as a test molecule, due to its smaller size and, therefore, lower computational cost. The relaxed xyz-geometry for this molecule, with a C-H bond length of $r_{\text{CH}} = 1.097 \text{ \AA}$, is available on the Octopus homepage. The total angle-integrated photoemission intensity spectrum has been converged fully for the radius $R = 8.5 \text{ \AA}$ (spherical box), mesh grid spacing $h = 0.24 \text{ \AA}$ and thickness of the absorbing boundary region $R_{\text{ABC}} = 3 \text{ \AA}$ (height of complex absorbing potential is -0.75). Positioning the surface detector far enough from the molecule, none of these parameters showed any influence on the low kinetic energy emissions. A convergence test has also been performed for the detector distance and the results are presented in Figure 28. First, we notice the considerable dependence of the low the kinetic energy contributions on the detector distance. In fact, this parameter seems to be the single most important factor when trying to converge these emissions out of the spectrum. Considering the contributions at the HOMO and HOMO-1 energies only, a detector distance of $> 5 \text{ \AA}$ should be sufficient for convergence. However, it takes at least 7 \AA to largely suppress the low kinetic energy contributions. We define the border between low kinetic energy emissions and emissions from the HOMO-1 and above at $E_{\text{kin.}}^{\text{LK}} = 11 \text{ eV}$.

Suppose the orbital Kohn-Sham wavefunctions are not fully spatial contained within the region inside the detector surface, due to a possibly too small detector distance. Then, at the detector surface, there is still a not insignificant part of the wavefunction being projected out at each point in time, contributing unphysical emissions by this technically still bound electron density. Pushing the surface detector further away from the molecule would then, if this hypothesis is holds, drastically reduce the intensity of these emissions as the orbital wavefunction falls off fast enough to be fully contained inside the detector region. An oscillation in the wavefunction induced by

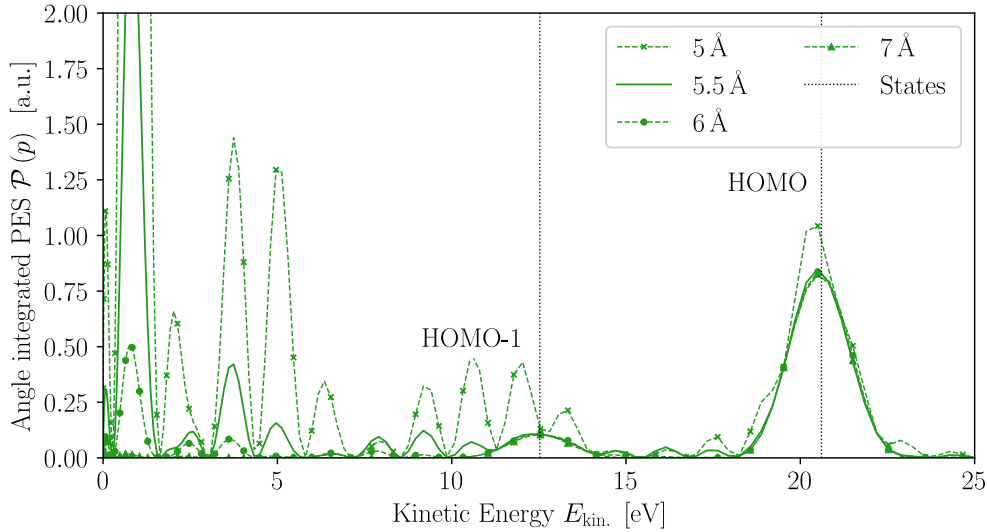


Figure 28: Total angle-integrated photoemission intensity of methane for different distances of the surface detector (solid and dashed green lines). Dotted lines are the kinetic energies corresponding to the two upper most orbitals HOMO-1 and HOMO. Computational details for this calculations: pump pulse energy $\omega_{\text{pu.}} = 2 \text{ eV}$, pump pulse maximum field strength $E_0^x = 0.5 \text{ mau}$, pump pulse period $T = 3 \text{ fs}$, probe pulse energy $\omega_{\text{pr.}} = 30 \text{ eV}$, probe pulse maximum field strength $E_0^x = 0.38 \text{ mau}$, probe pulse period $T = 3 \text{ fs}$, box radius $R = 14 \text{ \AA}$, mesh grid spacing $h = 0.28 \text{ \AA}$, width of absorbing boundary region $R_{\text{ABC}} = 5 \text{ \AA}$, time step $\Delta t = 0.0038 \text{ fs}$. Both pump and probe pulse have been \sin^2 -shaped with no delay for the full simulation period of $T = 3 \text{ fs}$.

an external electric field should then also be detectable as a oscillation in the time-dependent photoemission intensity, as this oscillation periodically changes the value of the wavefunction at the detector surface. This could also explain the dependence of the emissions on the pump field strength observed in Figure 19.

To test this hypothesis, we picked a detector distance of 5.5 \AA , as we observe both a converged spectrum for energies above the boundary and, also, still significant low kinetic energy emissions at this distance. However, see the oscillations described above in the photoemission data, requires time-resolution in the photoemission spectrum. The software package used for t-SURFF photoemission simulations Octopus has no such option implemented as of version 11.4. Therefore, the full simulation period of $T = 3 \text{ fs}$ has been sub-divided into 563 simulations with a simulation period of $\Delta T = 0.0054 \text{ fs}$. After each simulation the angle- and energy-integrated photoemission intensity up to a

kinetic energy of $E_{\text{kin.}}^{\text{LK}} = 11 \text{ eV}$ has been calculated. The result is a time-resolved photoemission intensity of the low kinetic energy contributions and is displayed for different variations, together with the laser setup and the HOMO→HOMO projections, in Figure 29. The radius of the simulation box

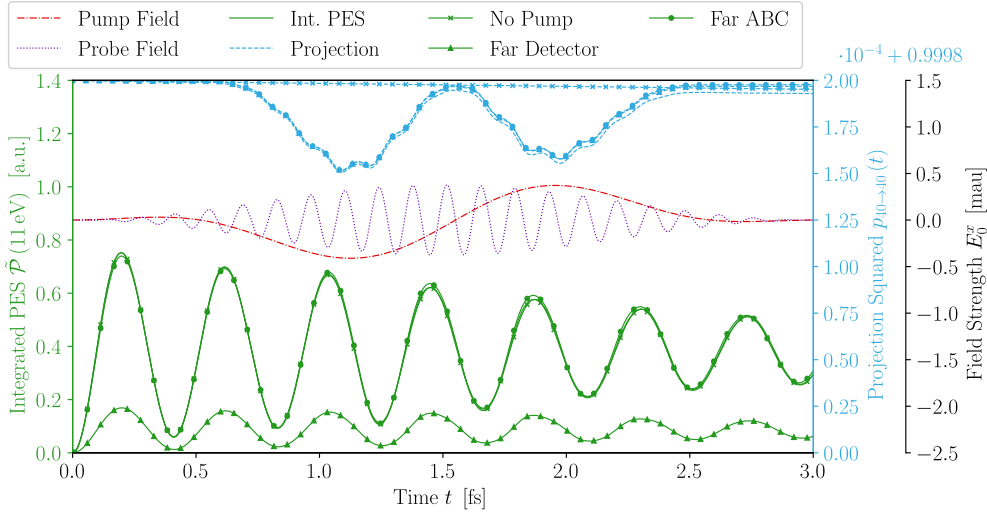


Figure 29: Angle-integrated photoemission intensity up to a kinetic energy of $E_{\text{kin.}}^{\text{LK}} = 11 \text{ eV}$ (solid green lines), laser setup (dashed red and purple dotted lines) and HOMO→HOMO projection (dashed blue lines) for different variations on the calculation “Int. PES” (no markers; see text). “No Pump” has no pump field, “Far Detector” places the detector surface and begin of the absorbing boundary region at 6 \AA and “Far ABC” moves the absorbing boundary region to 7 \AA while keeping the detector distance fixed.

has been $R = 8.5 \text{ \AA}$ with an increase to $R = 9 \text{ \AA}$ and $R = 10 \text{ \AA}$ for “Far Detector” and “Far ABC” to accommodate for increased in distance of detector surface and absorbing boundary condition, respectively. A mesh grid spacing of $h = 0.24 \text{ \AA}$, a time step of $\Delta t = 0.0027 \text{ fs}$ and identical laser setup to the convergence tests has been used.

In the time-resolved photoemission data we observe, according to the expectation resulting from the hypothesis, a damped periodic oscillation with a single frequency of $f = 2.3 \pm 0.3 \text{ fs}^{-1} \hat{=} 9 \pm 1 \text{ eV}$, where the uncertainty given is the uncertainty from the discrete Fourier Transform. This frequency, contrary to our hypothesis, does not fit either of the laser frequencies $\omega_{\text{pu.}} = 2 \text{ eV}$ and $\omega_{\text{pr.}} = 30 \text{ eV}$. However, it is close to the eigenenergy $E_{\text{H}} = -9.5 \text{ eV}$ of the HOMO state, although the high uncertainty resulting from the relatively short total simulation time does not allow for a very robust association. The

oscillation seen could, then, be explained simply by the time-evolution operator

$$\varphi_{\text{H}}(t) = \hat{U} \varphi_{\text{H}}(0) = e^{-iE_{\text{H}}t} \varphi_{\text{H}}(0).$$

Even though the oscillation due to the time-dependent Schrödinger equation for each orbital could still support the core of the hypothesis, that the orbital wavefunction is not fully contained inside the detector surface and is therefore projected out at each time step, it does not explain the complete absence of any dependence on the pump field we determined a consequence of our hypothesis and was also observed in the “No Pump” calculation in Figure 19. The only influence the photoemission intensity we observed here, is the detector radius (“Far Detector”) and only on the intensity itself, not the frequency of the oscillation. To determine the origin of the low kinetic energy contribution, and with it maybe a way to mitigate them easily, further simulations are needed. We suggest an increase in total simulation time to decrease the uncertainty in the frequency of the oscillation. Although costly, this should help to nail down or refute the link between the orbital eigenenergy and the oscillation frequency. Furthermore, simulations with highly non-spherical frontier orbitals and careful detector placement could show, whether the bulk of these low kinetic energy emissions results from where the orbital wavefunctions are closest to the detector surface.

D Octopost

“Octopost” is an open-source and free Python module which has been developed in the course of this Masters’s thesis and which combines a number of useful methods for routine tasks regarding data analysing after a (TD-)DFT calculation with the open-source code Octopus (see Chapter 3.1.1). This includes angle-resolved photoemission spectra and k-maps of periodic and non-periodic systems, orbital, band or atom projected density of states and bandstructures. The module is easy to use and allows for a quick first post-processing with built-in visualization options. In particular, the ARPES part of Octopost has been used extensively throughout this work, both in the simulation work itself and for the creation of the plots in this thesis.

As part of thesis, I helped to create Octopost out of a collection of in the working group pre-existing scripts and code fragments, predominately written by Christian Kern, a PhD student in the electronic structure theory group of Peter Puschnig. Octopost is available on GitLab (<https://gitlab.com/ckern/octopost>) and the PyPI index, includes a written documentation (<https://octopost.readthedocs.io>) and comes with demo scripts for most functionality provided by the module.

List of Figures

1	4-Amino-4'-nitrobiphenyl	7
2	Frontier orbitals of 4-Amino-4'-nitrobiphenyl	8
3	Analytic Rabi oscillation for different detunements	26
4	Rabi oscillation without RWA	28
5	Linear-response of the uncharged molecule	37
6	Spacing convergence in the linear-response calculation	38
7	Grid spacing convergence of the time-propagation linear-response calculation	39
8	HOMO→LUMO projection during resonant optical excitation	41
9	Dipole moment during optical excitation	42
10	Rabi oscillations for an extended time propagation	43
11	Spectral density of extended time calculation	44
12	Excitation with a laser tuned to the energy gap directly . . .	45
13	Influence of the field strength on the Rabi oscillation	45
14	Linear relationship between field strength and Rabi period/-maximum HOMO→LUMO excitation	46
15	Linear-response of the charged molecule	48
16	Excitation of the charged system (spin-unpolarized)	49
17	Excitation of the charged system (spin-polarized)	50
18	Pump-probe laser setup	52
19	Energy-dependent photoemission intensity	53
20	Energy-dependent photoemission intensity projected onto the HOMO state	54
21	k-maps at the HOMO energy	56
22	k-maps at the LUMO energy	57
23	Comparison of k-maps between TD-DFT and PW	59
24	Energy-dependent photoemission intensity for the ANBP cation	61
25	k-maps for the ANBP cation	62
26	k-map for charged molecule at a particular kinetic energy . . .	63
27	Ehrenfest dynamics influence on bond length and HOMO→LUMO transition	65
28	Low kinetic energy contributions convergence with detector distance	76
29	Time-resolved photoemission intensity of the low kinetic energy emissions	77

References

- [1] Puschnig, P. *et al.* Reconstruction of molecular orbital densities from photoemission data. *Science* **326**, 702–706 (2009).
- [2] Lüftner, D. *et al.* Imaging the wave functions of adsorbed molecules. *Proceedings of the National Academy of Sciences* **111**, 605–610 (2013).
- [3] Weiß, S. *et al.* Exploring three-dimensional orbital imaging with energy-dependent photoemission tomography. *Nature Communications* **6** (2015).
- [4] Haags, A. *et al.* Kekulene: On-surface synthesis, orbital structure, and aromatic stabilization. *ACS Nano* **14**, 15766–15775 (2020).
- [5] Haags, A. *et al.* Momentum space imaging of σ orbitals for chemical analysis. *Science Advances* **8** (2022).
- [6] Egger, L. *et al.* Charge-promoted self-metalation of porphyrins on an oxide surface. *Angewandte Chemie International Edition* **60**, 5078–5082 (2021).
- [7] Wallauer, R. *et al.* Tracing orbital images on ultrafast time scales. *Science* **371**, 1056–1059 (2021).
- [8] De Giovannini, U., Hübener, H. & Rubio, A. A first-principles time-dependent density functional theory framework for spin and time-resolved angular-resolved photoelectron spectroscopy in periodic systems. *Journal of Chemical Theory and Computation* **13**, 265–273 (2017). PMID: 27981832.
- [9] Sholl, D. S. & Steckel, J. A. *Density Functional Theory: A Practical Introduction* (Wiley, 2009).
- [10] Fiolhais, C., Nogueira, F. & Marques, M. A. L. *Primer in Density Functional Theory* (Springer London, Limited, 2008).
- [11] Marques, M. A., Maitra, N. T., Nogueira, F. M., Gross, E. & Rubio, A. *Fundamentals of Time-Dependent Density Functional Theory* (Springer-Verlag GmbH, 2012).
- [12] Hohenberg, P. & Kohn, W. Inhomogeneous electron gas. *Physical Review* **136**, B864–B871 (1964).
- [13] Yip, S. *Handbook of Materials Modeling* (Springer, 2005).
- [14] Kohn, W. & Sham, L. J. Self-consistent equations including exchange and correlation effects. *Phys. Rev.* **140**, A1133–A1138 (1965).
- [15] Stowasser, R. & Hoffmann, R. What do the kohn-sham orbitals and eigenvalues mean? *Journal of the American Chemical Society* **121**, 3414–3420 (1999).
- [16] Janak, J. F. Proof that $\frac{\partial \epsilon}{\partial n_i} = \epsilon$ in density-functional theory. *Physical Review B* **18**, 7165–7168 (1978).
- [17] Kohn, W. & Sham, L. J. Quantum density oscillations in an inhomoge-

- neous electron gas. *Phys. Rev.* **137**, A1697–A1705 (1965).
- [18] Marx, D. & Hutter, J. *Modern methods and algorithms of quantum chemistry*, chap. Ab Initio Molecular Dynamics: Theory and Implementation, 301 (2000).
- [19] Runge, E. & Gross, E. K. U. Density-functional theory for time-dependent systems. *Physical Review Letters* **52**, 997–1000 (1984).
- [20] Marques, M. A., Ullrich, C. A., Nogueira, F., Rubio, A. & Burke, K. *Time-Dependent Density Functional Theory* (Springer-Verlag GmbH, 2006).
- [21] Ullrich, C. *Time-dependent density-functional theory* (Oxford University Press, 2012).
- [22] Casida, M. E. Time-dependent density functional response theory for molecules 155–192 (1995).
- [23] Oliveira, M. J. T., Castro, A., Marques, M. A. L. & Rubio, A. On the use of neumann's principle for the calculation of the polarizability tensor of nanostructures. *Journal of Nanoscience and Nanotechnology* **8**, 3392–3398 (2008).
- [24] Dil, J. H. Spin and angle resolved photoemission on non-magnetic low-dimensional systems. *Journal of Physics: Condensed Matter* **21**, 403001 (2009).
- [25] Pohl, A., Reinhard, P.-G. & Suraud, E. Towards single-particle spectroscopy of small metal clusters. *Physical Review Letters* **84**, 5090–5093 (2000).
- [26] Giovannini, U. D. *et al.* Ab initio angle- and energy-resolved photoelectron spectroscopy with time-dependent density-functional theory. *Physical Review A* **85**, 062515 (2012).
- [27] Dauth, M. & Kümmel, S. Predicting photoemission intensities and angular distributions with real-time density-functional theory. *Physical Review A* **93**, 022502 (2016).
- [28] Tao, L. & Scrinzi, A. Photo-electron momentum spectra from minimal volumes: the time-dependent surface flux method. *New Journal of Physics* **14**, 013021 (2012).
- [29] Wopperer, P., Giovannini, U. D. & Rubio, A. Efficient and accurate modeling of electron photoemission in nanostructures with TDDFT. *The European Physical Journal B* **90** (2017).
- [30] Wolkow, D. M. Über eine klasse von lösungen der diracschen gleichung. *Zeitschrift für Physik* **94**, 250–260 (1935).
- [31] Saalman, U. & Schmidt, R. Non-adiabatic quantum molecular dynamics: basic formalism and case study. *Zeitschrift für Physik D Atoms, Molecules and Clusters* **38**, 153–163 (1996).
- [32] Peter Van Der Straten, H. M. *Atoms and Molecules Interacting with*

- Light: Atomic Physics for the Laser Era* (CAMBRIDGE, 2016).
- [33] Hohenester, U. *Nano and Quantum Optics* (Springer International Publishing, 2020).
 - [34] Morinaga, M. Deriving the static interaction between electric dipoles via the quantum gauge transformation (2013).
 - [35] Griffiths, D. *Introduction to quantum mechanics* (Prentice Hall, Englewood Cliffs, N.J, 1995).
 - [36] Novotny, L. & Hecht, B. *Principles of Nano-Optics* (Cambridge University Press, 2012).
 - [37] Ruggenthaler, M. & Bauer, D. Rabi oscillations and few-level approximations in time-dependent density functional theory. *Physical Review Letters* **102**, 233001 (2009).
 - [38] Fuks, J. I., Helbig, N., Tokatly, I. V. & Rubio, A. Nonlinear phenomena in time-dependent density-functional theory: What rabi oscillations can teach us. *Phys. Rev. B* **84**, 075107 (2011).
 - [39] Mollow, B. R. Power spectrum of light scattered by two-level systems. *Phys. Rev.* **188** (1969).
 - [40] Jokar, J. *Adiabatische Näherungen in zeitabhängiger Dichtefunktionaltheorie für den nicht-linearen Bereich*. Ph.D. thesis, RWTH Aachen University (2017).
 - [41] Marques, M. A. L., Castro, A., Bertsch, G. F. & Rubio, A. octopus: a first-principles tool for excited electron–ion dynamics. *Computer Physics Communications* **151**, 60–78 (2003).
 - [42] Mortensen, J. J., Hansen, L. B. & Jacobsen, K. W. Real-space grid implementation of the projector augmented wave method. *Physical Review B* **71**, 035109 (2005).
 - [43] Andrade, X. *et al.* Real-space grids and the octopus code as tools for the development of new simulation approaches for electronic systems. *Physical Chemistry Chemical Physics* **17**, 31371–31396 (2015).
 - [44] Tancogne-Dejean, N. *et al.* Octopus, a computational framework for exploring light-driven phenomena and quantum dynamics in extended and finite systems. *The Journal of Chemical Physics* **152**, 124119 (2020).
 - [45] Andrade, X., Botti, S., Marques, M. A. L. & Rubio, A. Time-dependent density functional theory scheme for efficient calculations of dynamic (hyper)polarizabilities. *The Journal of Chemical Physics* **126**, 184106 (2007).
 - [46] Sternheimer, R. On nuclear quadrupole moments. *Physical Review* **84**, 244–253 (1951).
 - [47] De Giovannini, U., Larsen, A. H. & Rubio, A. Modeling electron dynamics coupled to continuum states in finite volumes with absorbing boundaries. *The European Physical Journal B* **88**, 56 (2015).

- [48] Car, R. & Parrinello, M. Unified approach for molecular dynamics and density-functional theory. *Physical Review Letters* **55**, 2471–2474 (1985).
- [49] Lehtola, S., Steigemann, C., Oliveira, M. J. & Marques, M. A. Recent developments in libxc — a comprehensive library of functionals for density functional theory. *SoftwareX* **7**, 1–5 (2018).
- [50] Andrade, X. *et al.* Time-dependent density-functional theory in massively parallel computer architectures: the octopus project. *Journal of Physics: Condensed Matter* **24**, 233202 (2012).
- [51] Hartwigsen, C., Goedecker, S. & Hutter, J. Relativistic separable dual-space gaussian pseudopotentials from h to rn. *Physical Review B* **58**, 3641–3662 (1998).
- [52] Pueyo, A. G., Marques, M. A. L., Rubio, A. & Castro, A. Propagators for the time-dependent kohn–sham equations: Multistep, runge–kutta, exponential runge–kutta, and commutator free magnus methods. *Journal of Chemical Theory and Computation* **14**, 3040–3052 (2018).
- [53] Enkovaara, J. *et al.* Electronic structure calculations with GPAW: a real-space implementation of the projector augmented-wave method. *Journal of Physics: Condensed Matter* **22**, 253202 (2010).
- [54] Larsen, A. H. *et al.* The atomic simulation environment—a python library for working with atoms. *Journal of Physics: Condensed Matter* **29**, 273002 (2017).
- [55] Bahn, S. & Jacobsen, K. An object-oriented scripting interface to a legacy electronic structure code. *Computing in Science & Engineering* **4**, 56–66 (2002).
- [56] Walter, M. *et al.* Time-dependent density-functional theory in the projector augmented-wave method. *The Journal of Chemical Physics* **128**, 244101 (2008).
- [57] Blöchl, P. E. Projector augmented-wave method. *Physical Review B* **50**, 17953–17979 (1994).
- [58] Blöchl, P. E., Först, C. J. & Schimpl, J. Projector augmented wave method: ab initio molecular dynamics with full wave functions. *Bulletin of Materials Science* **26**, 33–41 (2003).
- [59] Briggs, E. L., Sullivan, D. J. & Bernholc, J. Real-space multigrid-based approach to large-scale electronic structure calculations. *Physical Review B* **54**, 14362–14375 (1996).
- [60] Dudarev, S. L., Botton, G. A., Savrasov, S. Y., Humphreys, C. J. & Sutton, A. P. Electron-energy-loss spectra and the structural stability of nickel oxide: An LSDA+u study. *Physical Review B* **57**, 1505–1509 (1998).
- [61] Hüser, F., Olsen, T. & Thygesen, K. S. Quasiparticle GW calculations

- for solids, molecules, and two-dimensional materials. *Physical Review B* **87**, 235132 (2013).
- [62] Onida, G., Reining, L. & Rubio, A. Electronic excitations: density-functional versus many-body green's-function approaches. *Reviews of Modern Physics* **74**, 601–659 (2002).
- [63] Sprangle, P. & Hafizi, B. High-power, high-intensity laser propagation and interactions. *Physics of Plasmas* **21**, 055402 (2014).
- [64] Puschnig, P. Organic Molecule Database: a database for molecular orbitals of π -conjugated organic molecules based on the atomic simulation environment (ASE) and NWChem as the DFT calculator (2020). URL <http://143.50.77.12:5000/>.
- [65] Brandstetter, D., Yang, X., Lüftner, D., Tautz, F. S. & Puschnig, P. kMap.py: A python program for simulation and data analysis in photoemission tomography. *Computer Physics Communications* **263**, 107905 (2021).
- [66] Barclay, M. S., Elles, C. G. & Caricato, M. On the discrepancy between experimental and calculated raman intensities for conjugated phenyl and thiophene derivatives. *The Journal of Physical Chemistry A* **124**, 4678–4689 (2020).